Monthly Notices of the ROYAL ASTRONOMICAL SOCIETY

MNRAS **454,** 2–27 (2015) doi:10.1093/mnras/stv1711

Tables of phase functions, opacities, albedos, equilibrium temperatures, and radiative accelerations of dust grains in exoplanets

J. Budaj,[1,2]★ M. Kocifaj,[3] R. Salmeron[1] and I. Hubeny[4]

[1]*Research school of Astronomy and Astrophysics, Australian National University, Canberra, ACT 2611, Australia*
[2]*Astronomical Institute, Slovak Academy of Sciences, 059 60 Tatranska Lomnica, Slovak Republic*
[3]*Faculty of Mathematics, Physics and Informatics, Comenius University, Mlynska dolina, 842 48 Bratislava, Slovak Republic*
[4]*Steward Observatory, University of Arizona, 933 N. Cherry Ave., Tucson, AZ, 85721, USA*

Accepted 2015 July 24. Received 2015 July 19; in original form 2014 October 3

ABSTRACT

There has been growing observational evidence for the presence of condensates in the atmospheres and/or comet-like tails of extrasolar planets. As a result, systematic and homogeneous tables of dust properties are useful in order to facilitate further observational and theoretical studies. In this paper we present calculations and analysis of non-isotropic phase functions, asymmetry parameter (mean cosine of the scattering angle), absorption and scattering opacities, single scattering albedos, equilibrium temperatures, and radiative accelerations of dust grains relevant for extrasolar planets. Our assumptions include spherical grain shape, Deirmendjian particle size distribution, and Mie theory. We consider several species: corundum/alumina, perovskite, olivines with 0 and 50 per cent iron content, pyroxenes with 0, 20, and 60 per cent iron content, pure iron, carbon at two different temperatures, water ice, liquid water, and ammonia. The presented tables cover the wavelength range of 0.2–500 μm and modal particle radii from 0.01 to 100 μm. Equilibrium temperatures and radiative accelerations assume irradiation by a non-blackbody source of light with temperatures from 7000 to 700 K seen at solid angles from 2π to 10^{-6} sr. The tables are provided to the community together with a simple code which allows for an optional, finite, angular dimension of the source of light (star) in the phase function.

Key words: opacity – scattering – astronomical data bases: miscellaneous – planets and satellites: atmospheres – circumstellar matter.

1 INTRODUCTION

Many classes of astronomical objects have low-enough temperature and high-enough density that grains of condensates can be formed. Such grains are usually called 'dust', although some authors use the more generic term 'condensates'. These objects include interstellar or interplanetary medium, molecular clouds, the outer regions of active galactic nuclei discs, outer atmospheres of cool stars (e.g. Mira-type supergiants), supernova remnants, brown dwarfs, extrasolar planets, circumstellar, protoplanetary, and debris discs, comets, and others.

The optical properties of condensates may not only influence but fully govern the emerging spectrum and structure of the object. Dust can absorb the impinging radiation and convert it directly into heating of the grains. This process is called 'absorption' or 'true absorption' to emphasize that the photon is thermalized. It is quantified by the absorption opacity. Dust can also scatter radiation in a process called 'scattering' without being heated. This process is characterized by the scattering opacity. Furthermore, scattering can be highly asymmetric, a property that is described by means of the phase function, which depends on the scattering angle (the deflection angle from the original direction of the impinging radiation). The most prominent feature is a strong forward scattering for large values of $x = 2\pi a/\lambda$ where a is particle size (radius) and λ is wavelength. Finally, condensation affects the chemical composition of the object. It removes the condensed elements from the gas phase within the dust cloud and, in the atmosphere, also from the region above the clouds due to the rain-out.

This paper focuses mainly on extrasolar planets. Extrasolar planets (exoplanets) are found at a wide range of orbital periods and/or distances from their host stars, ranging from a fraction of a day to many years. Their hosts have spectral types from A-stars to M-stars and down to brown dwarfs. As a result, depending on the amount of stellar irradiation, the atmospheres of exoplanets may have temperatures from a few thousand K to about one hundred K. At such temperatures condensates are expected to be present in their atmospheres or circumplanetary material. Condensates are usually

★ E-mail: budaj@ta3.sk

confined to clouds at a certain depth or region according to their condensation temperatures (see e.g. Ackerman & Marley 2001; Allard et al. 2001; Tsuji 2002; Lodders 2003; Sánchez-Lavega, Pérez-Hoyos & Hueso 2004; Burrows, Sudarsky & Hubeny 2006; Lodders & Fegley 2006; Helling et al. 2008; Morley et al. 2012, 2014). In highly irradiated atmospheres, or at large depths of cooler exoplanets, only the most refractory dust species (Ca–Al–Ti bearing compounds) can survive. They are overlaid by the optically opaque clouds of iron and various silicates. Higher up in the atmosphere, or at cooler temperatures, finer sulphide and alkali halide clouds may be present. Water clouds become dominant at lower temperatures and, at even lower temperatures, ammonia clouds are expected. An entire classification scheme for exoplanets was proposed by Sudarsky, Burrows & Pinto (2000) based on the expected effects of such clouds on their spectra.

The above-mentioned dust phase function should not be confused with the planet phase function. The later describes the light curve of a planet as a function of orbital phase and is modulated by the dust phase function. There are numerous theoretical studies and numerical models of the light curves, spectra, planet phase functions, and albedos in extrasolar planets including the effect of clouds (Marley et al. 1999; Seager, Whitney & Sasselov 2000; Sudarsky et al. 2005; Cahoy, Marley & Fortney 2010; Kane & Gelino 2011). A convenient analytical model for albedos and phase curves taking into account non-isotropic scattering was presented in Madhusudhan & Burrows (2012) and Heng, Mendonça & Lee (2014). It turned out that hot Jupiters have very small albedos in comparison with the Solar system planets and it is quite difficult to detect them in reflected light in the optical region due to strong absorption in the Na, K resonance lines and/or absence of highly reflective condensate grains (Sudarsky et al. 2000; Rowe et al. 2008; Cowan & Agol 2011). Nevertheless, recent observations support the presence of clouds in their atmospheres. Pont et al. (2013) and Lee et al. (2014) state that transmission spectra of HD189733 are consistent with the presence of condensates in the atmosphere of this planet. Sing et al. (2013) argues that aerosols, especially corundum, may explain the transmission spectra of another hot Jupiter, WASP-12b. Wakeford & Sing (2015) examined the effect of various grain species and their particle sizes in the atmosphere of a typical hot Jupiter (HD189733b) on the transmission spectrum. They predicted strong enstatite and perovskite features in the infrared (IR) region. Also, the atmosphere of super-Earth GJ 1214b must contain clouds to be consistent with the observed transmission data (Howe & Burrows 2012; Morley et al. 2013; Kreidberg et al. 2014). Madhusudhan, Burrows & Currie (2011) concluded that directly imaged HR 8799 planets have thick clouds (thicker than those required to explain data for typical L and T dwarfs). On the other hand, Marley et al. (2012) suggested that it is because exoplanets have lower gravities which moves the clouds and the L to T spectral transition to lower effective temperatures than in brown dwarfs.

Forward scattering on dust can be particularly important in eclipsing systems during the primary eclipse, when a cool dusty object is in front of the main source of light (Budaj 2011). Recently a few such systems with dusty discs were discovered (Dong et al. 2014; Meng et al. 2014; Rattenbury et al. 2015). In extrasolar planets, this situation is exactly encountered near the transit. de Kok & Stam (2012) studied how forward scattering affects the transmission spectroscopy of exoplanetary atmospheres. However, dust clouds associated with planets are not necessarily confined to the atmosphere of the planet. Rappaport et al. (2012) discovered a transiting disintegrating exoplanet KIC12557548b with a comet-like dusty tail extending well beyond its Hill radius and featuring a pre-transit brightening. Recent studies have shown that pre-transit brightening is due to strong forward scattering and can be used, together with the colour dependence of the transit depth, to constrain the particle size of dust grains in the comet-like tail, which was found to be of the order of 1 μm (Budaj 2013; Croll et al. 2014; Bochinski et al. 2015, see also Brogi et al. 2012; van Werkhoven et al. 2014). Two other objects of this kind (KOI-2700b, EPIC201637175B) have been discovered already by Rappaport et al. (2014) and Sanchis-Ojeda et al. (2015). The observed tail lengths in these objects are consistent with corundum or iron-rich silicate dust grains (van Lieshout, Min & Dominik 2014). Finally, scattering on dust in the Earth atmosphere may have important effects on lunar eclipses or on the Earth transmission spectrum (Kocifaj 1994; Kocifaj & Horvath 2005; García Muñoz & Pallé 2011; García Muñoz et al. 2011; Pallé et al. 2011), as well as on the light curve and spectra of Earth (Tinetti et al. 2006; Stam 2008). A recent summary of the cloud and haze formation in exoplanet atmospheres can be found in Marley et al. (2013).

Radiative transfer calculations in planetary atmospheres are very CPU-time demanding. As a result, in many applications researchers use simplifying assumptions such as isotropic scattering or analytical Henyey–Greenstein dust phase functions given that more exact calculations require application of Mie theory or the use of additional Mie-scattering codes. In such cases, pre-computed dust opacities and phase functions may be very convenient and efficient (Hubeny & Lanz 1995; Burrows et al. 2006). The aim of this paper is to facilitate further research and provide the community with homogeneous and systematic tables of dust phase functions, opacities, single scattering albedos, grain equilibrium temperatures, and radiative accelerations relevant mainly for the field of extrasolar planets or circumplanetary (circumstellar) material. These tables can be incorporated into more complex cloud models, or find additional applications in brown dwarfs, protoplanetary discs, comets, and interacting binary stars.

The supplied tables may also be beneficial for analysis and interpretation of observations from future space missions. Large area planet transit surveys such as *TESS* (Ricker et al. 2014) and *PLATO* (Rauer et al. 2014) will discover many exoplanets that will be followed up by other large telescopes and their atmospheres, albedos, and phase curves studied (Deming et al. 2009). Superb photometric precision of *CHEOPS* (Broeg et al. 2013) will detect exoplanetary atmospheres and study day–night heat transfer in hot Jupiters, and their albedos. *JWST* (Gardner et al. 2006; Beichman et al. 2014) will perform transit or occultation spectroscopy and direct imaging of planets which will enable chemical composition analysis of the planetary atmospheres. It will study dust in all sorts of environments including our own Solar system or protoplanetary discs. Another mission, *ECHO*, dedicated to study the composition of atmospheres of transiting exoplanets was proposed (Tinetti et al. 2012, 2015).

Since there are currently no observational constraints on the shape, porosity, or aggregate structure of grains in these environments, we assume homogeneous spherical particles and Mie theory. Recently, Cuzzi, Estrada & Davis (2014) proposed an opacity model which takes into account porous aggregates, Mordasini (2014) developed an analytical model for grain opacity in the atmospheres of forming planets, and Ormel (2014) presented a method to include the evolution of grain size and opacity into the structure of protoplanetary atmospheres. The above-mentioned features are not contemplated in this paper and it was not our intention to calculate cloud or atmosphere models for exoplanets.

This paper is organized as follows. Section 2 describes the source of the refractive index. Section 3 describes the parameter space covered by the calculations. Sections 4 and 6 describe the calculations

and properties of the phase functions, opacities, albedos, equilibrium temperatures, and radiative accelerations of each species. Section 5 provides a detailed description of the tables, their format and units. Sections 7 contains our summary and conclusions.

2 COMPLEX REFRACTIVE INDEX

The optical properties (cross-sections for scattering, absorption, and phase functions) of spherical dust particles composed of a homogeneous material with a wavelength-dependent refractive index can be calculated using the conventional Mie theory. Here we describe the sources of the refractive index. The Heidelberg–Jena–St.Petersburg Database of Optical Constants is a very convenient starting point (Henning et al. 1999; Jäger et al. 2003a).

Corundum: it is the most common form of crystalline alumina (Al_2O_3), which is α alumina. It is one of the most refractory condensates that is expected to condense from a gas of solar chemical composition. Corundum is an optically anisotropic (birefringent) material. We adopted recent IR–mm measurements of its refractive index by Zeidler, Posch & Mutschke (2013). These are *in situ*, high temperature measurements, in the range of 300–928 K for both ordinary and extraordinary rays. The optical properties of corundum were found to be temperature dependent. Corundum is most important for exoplanets at high temperatures since at lower temperatures its effects are superseded by more opaque and less refractory species. For this reason, we adopted the measurements for the highest temperature considered in the above mentioned study (928 K). We calculated the optical properties (cross-sections, opacities, phase functions, asymmetry parameter) independently for both ordinary and extraordinary rays. Then we took a weighted sum of them with weights of 1/3 and 2/3 for extraordinary and ordinary rays, respectively, as discussed by Zeidler et al. (2013) to account for an averaged crystal orientation. There are several types of alumina which may differ in optical properties. Therefore we considered also γ alumina and its complex refractive index was taken from Koike et al. (1995). Their measurements are at room temperature and cover a broad range of wavelengths from UV, optical, to far-IR. If not otherwise specified, in the next, we will refer to γ alumina as alumina and α alumina as corundum.

Perovskite: perovskite is calcium titanium oxide (calcium titanate) with the chemical formula $CaTiO_3$. Similar to corundum, it is one of the most refractory species and the highest temperature condensates from a gas of solar chemical composition. It may form clouds in exoplanets and brown dwarfs (Lodders & Fegley 2006) which might be detected in the transmission spectrum in the IR region with instruments like *JWST* (Wakeford & Sing 2015). Formation of perovskite is interesting also because it removes titanium and thus also TiO from the gas phase. TiO gas is a major opacity source in the optical region of M dwarfs. If present, it would be a strong absorber also in exoplanets, causing temperature inversions – stratospheres (Hubeny, Burrows & Sudarsky 2003; Burrows, Budaj & Hubeny 2008; Knutson et al. 2008) with huge impact on the atmospheric structure and spectra. The complex refractive index of perovskite was taken from Posch et al. (2003). They made reflectance spectroscopy of a natural perovskite crystal and used Lorentz oscillator fits to determine the optimum parameters, such as frequencies, strengths, or damping constants. Lorentz oscillator parameters were used to compute optical constants n and k, that in turn pre-determine small particle spectra. Unfortunately, the dielectric constants obtained this way do not cover the whole spectral region and span only wavelengths longer than 2 μm.

Pyroxenes: the complex refractive index of pyroxenes was taken from Dorschner et al. (1995), who determined the optical constants from reflectance and transmittance measurements. While the reflectance data were available for wavelengths ranging from ≈0.2 to 500 μm with Kramers–Kronig analysis in 8–80 μm, the transmittance analysis was possible only at wavelengths below 8 μm and then above 100 μm. The quality of data sets was guaranteed by homogeneity tests made for the sample during lab experiments. The optical properties of pyroxene ($Mg_xFe_{1-x}SiO_3$) in the optical region are quite sensitive to the amount of iron $1 - x$ in the mineral. Therefore, we considered three kinds of pyroxenes: enstatite (iron free, $x = 1$), pyroxene with 20 per cent of iron ($x = 0.8$), and pyroxene with 60 per cent of Mg atoms replaced by iron ($x = 0.4$).

Olivines: forsterite (Mg_2SiO_4) was adopted as an iron-free representative of the olivine family of magnesium silicates. Its optical data were taken from Jäger et al. (2003b), who used sol–gel technique to produce amorphous magnesium silicates and followed with homogeneity and purity tests based on TEM analysis combined with EDX. We considered also an iron-enriched olivine ($Mg_{2y}Fe_{2-2y}SiO_4$) with half–half of Mg–Fe atoms ($y = 0.5$) and the data were taken from Dorschner et al. (1995).

Iron: in contrast to silicates, iron-like particles show different optical characteristics as discussed by Pollack et al. (1994), where the real and imaginary values of complex refractive index were published for wavelengths ranging from 0.1 to 10^5 μm. However, for pure iron we have used two data sources: Johnson & Christy (1974) for $\lambda < 0.7$ μm and Ordal et al. (1988) for $\lambda > 0.7$ μm. In both cases, the experimental data were collected at room temperature. For the metals, the Drude model – the classical phenomenological approach for the conductivity – is traditionally used to explain the transport properties of electrons. However, the Drude model is not well suited for the near- and mid-IR region, thus it may potentially be inaccurate when applied to $\lambda > 0.7$ μm. Nevertheless, Ordal et al. (1988) concluded that, within the experimental error, the non-resonant cavity data can be fit with plasma frequency 32 900 cm^{-1} and damping frequency 213 cm^{-1}. Combining their measurements with Kramers–Kronig analysis, the frequency-dependent refractive indices were computed and provided along with the reflectance data.

Carbon: carbon, mainly in the form of graphite particles, is an important ingredient of interstellar dust. It has not been detected in extrasolar planets, yet. Nevertheless, we included carbon dust particles into our tables since carbon grains are potentially abundant refractory species and might be present in circumstellar material, carbon-rich environments, or disintegrating exoplanets. The complex refractive index of carbon dust may be quite sensitive to the temperature due to the presence of free charge carriers at higher temperatures as shown by Jager, Mutschke & Henning (1998). These authors measured the optical properties of amorphous carbon for a set of temperatures ranging from 400 to 1000°C for a broad wavelength range from 0.2 to about 500 μm. As the temperature increased, an increased carbonization and graphitization of the sample was observed. We adopted their measurements at the highest and lowest temperatures.

Water: a new update of the water ice optical constants was published recently by Warren & Brandt (2008), who revised the imaginary part of the complex refractive index in the visible spectrum. The values they tabulated are appropriate for the hexagonal crystal form of ordinary ice or frozen water at temperatures not far below the melting point (the nominal temperature was 266 K). Regarding liquid water drops, the optical data published by the International Association for the Properties of Water and Steam are probably the most accurate, but are available only for the real part of the

refractive index and valid only for a limited spectral range. Therefore we have used Segelstein data (Segelstein 1981), which cover a much wider range of wavelengths for both real and imaginary values of the refractive index. Segelstein data are well accepted by the optical community and thus often used in simulating the optical properties of liquid water in various environments.

Ammonia: for ammonia (NH_3) at temperature ranging from 77 to 88 K we used Martonchik, Orton & Appleby (1984), which is the more comprehensive review of the optical constants of NH_3 ice. However, we stress that optical constants for solid ammonia in the cubic phase may differ significantly from those in other phases – as shown by Ferraro, Sill & Fink (1980).

3 PARAMETER SPACE – GRID

Particle size: we assumed homogeneous spherical particles with a poly-dispersed Deirmendjian particle size (radius) distribution (Deirmendjian 1964), n_r, given by

$$n_r = \left(\frac{r}{r_c}\right)^6 e^{-6\frac{r}{r_c}}, \quad (1)$$

where r_c is the critical or modal particle radius, where the function has its maximum. We truncate the size distribution at $0.22\,r_c$ for small particles and at $6\,r_c$ for large particles. Particular attention is paid to the extended tail of larger particles, since their contribution may be significant e.g. to the Rayleigh scattering or to the forward scattering peak. This particle size distribution is shown in Fig. 1. We define the distribution on a very fine integration step in order to average the phase functions and to suppress the ripple structure that would appear in the phase function of spherical mono-dispersed particles. For large particle sizes it is necessary to take into account as many as 1600 points in the particle size distribution. We calculate the dust optical properties for 21 particle size distributions with different modal radii ranging from 0.01 to 100 μm with an equidistant step of 0.2 dex in the logarithm of r_c. Such particle size distributions can be expected for example in planetary atmospheres. Note, however, that although the range of our particle size distribution (see Fig. 1) spans more than 1 dex, the typical full width at half-maximum of such a distribution is relatively narrow, about 0.5 dex. Consequently, our results obtained assuming a distribution with a certain modal radius might be used also as a representative values for particles with radii equal to the modal particle radius

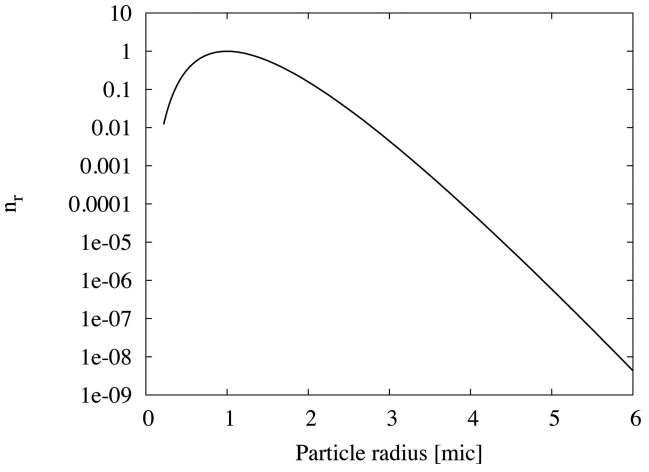

Figure 1. Deirmendjian particle size distribution with a modal particle size of 1 μm.

Table 1. Summary of the refraction index measurements adopted in this work.

Species	λ	*N*	ρ^g	Reference
Alumina	0.2–400	617	2.9	K
Corundum	6.7–1e4	1500	2.9	Z
Perovskite	2.0–5843	2000	4.1	P
Iron	0.19–1.9	49		J&C
Iron	0.62–286	53	7.874	O
Forsterite	0.20–949	4847	3.0	J03
Olivine50	0.20–500	109	3.0	D
Enstatite	0.20–500	109	3.0	D
Pyroxene20	0.20–500	109	3.0	D
Pyroxene60	0.20–500	109	3.0	D
Carbon1000	0.20–794	73	1.988	J98
Carbon0400	0.20–518	69	1.435	J98
Water ice	0.04–2e6	486	1.0	W&B
Water liq	0.01–1e7	1261	1.0	S
Ammonia	0.14–200	298	0.88	M

Notes. Type of grains; λ – wavelength range (μm); *N* – number of wavelength measurements; ρ^g – grain density ($g\,cm^{-3}$); Reference: K – Koike et al. (1995), Z – Zeidler et al. (2013), P – Posch et al. (2003), J&C – Johnson & Christy (1974), O – Ordal et al. (1988), J03 – Jäger et al. (2003b), D – Dorschner et al. (1995), J98 – Jager et al. (1998), W&B – Warren & Brandt (2008), S – Segelstein (1981), M – Martonchik et al. (1984).

and might be assembled to construct optional, broader, particle size distributions if necessary.

Wavelength coverage: optical properties are calculated for 400 frequency points covering the region 0.2–500 μm, and spaced equidistantly in logarithm of wavelength. This wavelength range covers most of the spectral energy distribution (SED) of stars with effective temperatures lower than ≈8000 K. Not always the entire wavelength region is covered by the measurements of the refraction index (see the Table 1 for summary).

Scattering angles: phase functions are calculated for 65 angles ranging from 0 to 180 deg. Since the scattering is not isotropic, and may have a very strong and narrow forward scattering peak, we adopt a much finer step in the forward and backward scattering regimes. Angles are symmetric with respect to 90 deg.

Dust species: optical properties of different condensates are calculated on the same grid of 21 particle size distributions and 400 wavelengths. They are corundum/alumina, perovskite, pure iron, forsterite as an iron-free representative of the olivine family of silicates, olivine with 50 per cent of iron, enstatite – an iron-free representative of the pyroxene family of silicates, pyroxenes with 20 and 60 per cent of iron, carbon at two different temperatures 1000 and 400°C, water ice, water liquid, and ammonia.

Star temperatures: in addition to inherent dust parameters (dust chemical composition, particle size), some grain properties (equilibrium grain temperature, radiative acceleration) depend also on the properties of the irradiating object. The most important property of the light source is its SED and its angular dimension (i.e. its size and distance). The SED on the surface of the source is mainly a function of its effective temperature and, to a lesser extent, also of the surface gravity, chemical composition, microturbulence and/or other free parameters. In the case of theoretical models, the output SED depends also on various simplifying assumptions and/or input data. For this reason, we calculated equilibrium grain temperatures for 13 star/brown dwarf effective temperatures: 7000, 5800, 5000, 4500, 4000, 3500, 3000, 2500, 2000, 1600, 1200, 900, and

700 K. For objects with temperatures ≤2500 K we assumed the surface gravity $\log g = 5.0$ (cgs), while for hotter objects we assumed $\log g = 4.5$ (cgs). The source is further assumed to have a solar chemical composition (Asplund et al. 2009; Caffau et al. 2011). We use a single homogeneous grid of synthetic spectra based on atmospheric model calculations, BT-Settl (CIFIST2011-2015, CIFIST2011; Allard et al. 2003; Baraffe et al. 2015), which covers the entire parameter space. These models are 1D, static, with spherical symmetry, in local thermodynamical equilibrium, with convection and take into account atomic, molecular, and dust opacities. The spectra list energy flux, F_λ, on the surface of the object in erg s^{-1} cm^{-2} cm^{-1} from 0.001 to 1000 μm. This can be easily converted to, F_ν, in units of erg s^{-1} cm^{-2} Hz^{-1} via $F_\nu = F_\lambda \lambda^2/c$. We recall that the effective temperature, $T_{\rm eff}$, of the object is, by definition, the temperature of the blackbody with the same total energy output i.e.

$$\int F_\nu {\rm d}\nu \equiv \sigma T_{\rm eff}^4 = \pi \int B_\nu(T_{\rm eff}){\rm d}\nu, \quad (2)$$

where σ is the Stefan–Boltzmann constant and B_ν is the Planck function.

Solid angles: the dust temperature depends also on the solid angle subtended by the source of light. We considered 15 values, roughly logarithmically spaced, ranging from 2π up to 10^{-6} sr. Radiative accelerations are calculated for the same stellar effective temperatures and particle sizes. Their dependence on the solid angle becomes insignificant at a relatively small distance from the source and thus was not included.

4 CALCULATIONS

4.1 Opacities

We use a widely available Mie scattering code CALLBHMIE adapted by B. T. Draine. It calls iteratively the Bohren–Huffman Mie scattering sub-routine BHMIE (Bohren & Huffman 1983, Appendix A). It provides $Q_{\rm a}$, $Q_{\rm s}$, and $Q_{\rm e}$, which are efficiency factors for absorption, scattering, and extinction, respectively, for particles with radius r. They are related to the $C_{\rm a}$ and $C_{\rm s}$, the absorption and scattering cross-sections, via

$$C_{\rm a} = Q_{\rm a}\pi r^2, \quad C_{\rm s} = Q_{\rm s}\pi r^2, \quad Q_{\rm e} = Q_{\rm a} + Q_{\rm s}. \quad (3)$$

It is assumed that the dust grains are composed of homogeneous material, have spherical shape, and are placed in an environment with the complex refractive index of 1-0i. The code is written in FORTRAN 77. It was modified to calculate the average cross-sections for absorption $\overline{C_{\rm a}}$ and scattering $\overline{C_{\rm s}}$ for an ensemble of particles with an optional size distribution n_r.

$$\overline{C_{\rm a}} = \frac{1}{n}\int C_{\rm a} n_r {\rm d}r \qquad \overline{C_{\rm s}} = \frac{1}{n}\int C_{\rm s} n_r {\rm d}r, \quad (4)$$

where

$$n = \int n_r {\rm d}r. \quad (5)$$

Subsequently, the absorption and scattering opacities $\kappa_\nu^{\rm dust}$, $\sigma_\nu^{\rm dust}$ of condensates in units of cm^{-1} are given by

$$\kappa_\nu^{\rm dust} = \overline{C_{\rm a}} n\ , \qquad \sigma_\nu^{\rm dust} = \overline{C_{\rm s}} n. \quad (6)$$

For practical applications it is more convenient to use the opacities per gram of dust material, given by

$$\kappa_{\nu,\rho}^{\rm dust} = \kappa_\nu^{\rm dust}/\rho_{\rm d}, \qquad \sigma_{\nu,\rho}^{\rm dust} = \sigma_\nu^{\rm dust}/\rho_{\rm d}, \quad (7)$$

where $\rho_{\rm d}$ is the density of dust made of particular species and $\kappa_{\nu,\rho}^{\rm dust}$, $\sigma_{\nu,\rho}^{\rm dust}$ are absorption and scattering opacities, respectively, per gram of dust material in units of cm^2 g^{-1}. The dust density can be expressed as

$$\rho_{\rm d} = \int M_r n_r {\rm d}r = \rho^{\rm g} \int V^{\rm g} n_r {\rm d}r = \rho^{\rm g} \overline{V^{\rm g}} n = \overline{M^{\rm g}} n, \quad (8)$$

where M_r is mass of a dust grain of radius r. $\overline{V^{\rm g}}$, $\overline{M^{\rm g}}$ are the mean volume and mass of a dust grain, respectively, and

$$\overline{M^{\rm g}} = \frac{\rho^{\rm g}}{n}\int V^{\rm g} n_r {\rm d}r = \frac{4\pi\rho^{\rm g}}{3n}\int r^3 n_r {\rm d}r. \quad (9)$$

In the above expression, $\rho^{\rm g}$ is the (constant) density of a grain of dust. Substituting equations (8) and (6) into equation (7) one can obtain the following relation between opacities and cross-sections:

$$\kappa_{\nu,\rho}^{\rm dust} = \frac{\overline{C_{\rm a}}}{\overline{M^{\rm g}}} \quad (10)$$

$$\sigma_{\nu,\rho}^{\rm dust} = \frac{\overline{C_{\rm s}}}{\overline{M^{\rm g}}}. \quad (11)$$

Using these opacities, the monochromatic optical depth along the line of sight z is then given by

$$\tau_\nu = -\int \rho_{\rm d}(z)[\kappa_{\nu,\rho}^{\rm dust}(z) + \sigma_{\nu,\rho}^{\rm dust}(z)]dz. \quad (12)$$

In the following, the sum of the absorption and scattering opacities will be referred to as a total opacity. Table 1 also lists the densities of dust grains, $\rho^{\rm g}$, which we assumed in the opacity calculations. Note that the density of corundum is ≈4 g cm^{-3} but since corundum is most interesting at high temperatures when other species are still in the gas phase, we adopted the density of corundum close to its melting point which is significantly lower, about 2.9 g cm^{-3}. On the contrary, the density of ammonia ice rises significantly with temperature, but reaches a plateau between 60–100 K at about 0.88 g cm^{-3} (Satorre et al. 2013), which is the value we adopted. The density of amorphous carbon was also found to increase significantly with temperature due to increasing graphitization. We adopted the densities from Jager et al. (1998) for the temperatures of 400 and 1000°C which correspond to those adopted for the complex refractive index.

4.2 Phase functions

We used the same code to calculate the S_{11} element of the scattering matrix for uniformly sized particles with radius r. S_{11} describes the angular distribution of the scattered light assuming that the incident light is unpolarized. It is convenient to normalize this angular distribution such that its integral over the whole solid angle ${\rm d}\omega = \sin(\alpha){\rm d}\alpha{\rm d}\phi$ is 4π. Such distribution is referred to as a phase function, $p(\alpha, r)$, where α is the scattering angle which measures the deflection from the original direction of the photon:

$$\int p(\alpha, r){\rm d}\omega = \int_0^{2\pi}\int_0^{\pi} p(\alpha, r)\sin(\alpha){\rm d}\alpha{\rm d}\phi = 4\pi. \quad (13)$$

The phase function of the population of particles, $\overline{p}(\alpha)$, with the size distribution n_r, can be calculated in the following way:

$$\overline{p}(\alpha) = \int p(\alpha, r) C_{\rm s} n_r {\rm d}r/(\overline{C_{\rm s}} n). \quad (14)$$

Since $C_{\rm s} n_r$ does not depend on direction, the averaged phase function $\overline{p}$ has the same normalization.

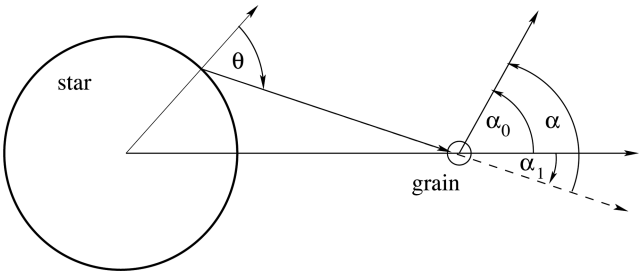

Figure 2. Definition of the geometry and angles.

The mean cosine of the scattering angle g, also known as the asymmetry parameter, is calculated from the normalized polydispersed phase function as

$$g = \int \overline{p}(\alpha)\cos(\alpha)\mathrm{d}\omega \,/\, \int \overline{p}(\alpha)\mathrm{d}\omega. \tag{15}$$

Once the opacities are known, the thermal emissivity of condensates (energy per unit time, frequency, volume, and solid angle) associated with its true absorption can be calculated as

$$\epsilon_\nu^{\mathrm{th,dust}} = B_\nu(T)\rho_\mathrm{d}\kappa_{\nu,\rho}^{\mathrm{dust}}, \tag{16}$$

where B_ν is the Planck function. The angle-dependent scattering emissivity of condensates into a direction α_0 can be calculated from the scattering opacity and phase function via the following expression:

$$\epsilon_\nu^{\mathrm{sc,dust}}(\alpha_0) = \iint p[\alpha(\alpha_0,\alpha_1), r]C_s n_r I_\nu[\theta(\alpha_1,\phi)]\mathrm{d}r\mathrm{d}\omega/(4\pi) \tag{17}$$

or

$$\epsilon_\nu^{\mathrm{sc,dust}}(\alpha_0) = \int \overline{p}(\alpha)\rho_\mathrm{d}\sigma_{\nu,\rho}^{\mathrm{dust}} I_\nu \mathrm{d}\omega/(4\pi), \tag{18}$$

where $I_\nu[\theta(\alpha_1,\phi)]$ is the specific intensity of radiation coming from the direction (α_1,ϕ) with solid angle $\mathrm{d}\omega = \sin(\alpha_1)\mathrm{d}\alpha_1\mathrm{d}\phi$, see Fig. 2. It is usually determined by solving the transfer equation as a function of angle $\theta = \theta(\alpha_1,\phi)$ with respect to the normal to the surface of the object. In the following we will write the specific intensity simply as I_ν. One can define another averaged phase function, P_DA such that

$$P_\mathrm{DA}(\alpha_0) = \frac{\int \overline{p}(\alpha)I_\nu\mathrm{d}\omega}{\int I_\nu\mathrm{d}\omega} = \frac{\int \overline{p}(\alpha)I_\nu\mathrm{d}\omega}{4\pi J_\nu}, \tag{19}$$

where J_ν is the mean intensity given by

$$J_\nu = \int I_\nu\mathrm{d}\omega/(4\pi). \tag{20}$$

This phase function is an average over the source of light. Since intensity depends on the angle, equation (19) does not guarantee that P_DA is normalized, contrary to e.g. $p(\alpha, r)$. However, using P_DA, the scattering emission can be expressed in a very simple way as

$$\epsilon_\nu^{\mathrm{sc,dust}}(\alpha_0) = P_\mathrm{DA}(\alpha_0)\rho_\mathrm{d}\sigma_{\nu,\rho}^{\mathrm{dust}} J_\nu. \tag{21}$$

If we consider a distinct source of light, such as a star for example, and a medium surrounding the source and our dust grain, which is optically thin, or if we are assuming single scattering events, then P_DA is an average of the phase function over the surface of the star and α_0 can be conveniently measured from the ray originating at the centre of the star. If the star is far or if it is small, then P_DA equals $\overline{p}$. However, if the star has a non-negligible angular

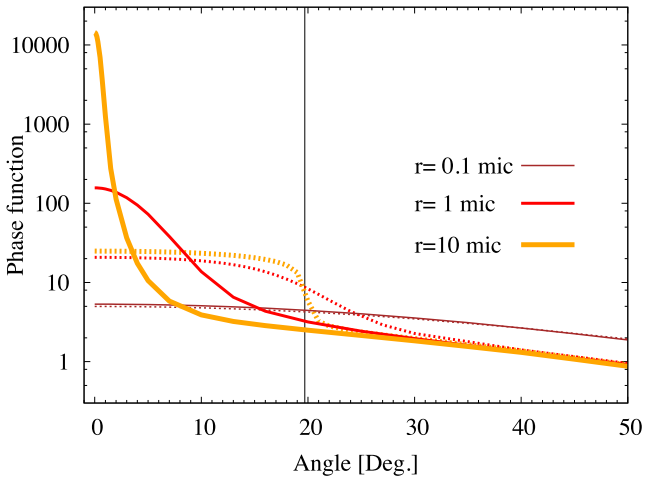

Figure 3. Comparison of phase functions assuming a point source of light (solid lines) versus the phase functions that take into account the finite dimension of the stellar disc (dotted lines). Example is for enstatite at 600 nm for different dust particle radii. Dotted line for 0.1 μm particles almost coincides with the solid line. The vertical line illustrates the angular radius of the stellar disc of WASP103 as seen from the planet WASP103b (Gillon et al. 2014; Southworth et al. 2015).

dimension on the sky, compared to the characteristic changes in the phase function, then one has to take its angular dimension into account. The phase function of large grains or at short wavelengths usually has a very strong forward-scattering peak, which can be much sharper than the stellar disc as seen e.g. from a typical hot Jupiter or a close in extrasolar planet. To take this effect into account one has to split the stellar disc into elementary surfaces and integrate the phase function over the disc as in the equation (19). In doing so we assume a quadratic limb darkening of the stellar surface:

$$I_\nu = I_\nu(0)[1 - u_1(1-\cos\theta) - u_2(1-\cos\theta)^2], \tag{22}$$

where $I_\nu(0)$ is intensity perpendicular to the surface of the source and θ is angle between the line of sight and a normal to the surface.

One has to be cautious and calculate the phase functions with a very fine step near the zero angle because of the strong forward scattering and, consequently, the disc-averaged phase function with a very fine step near the edge of the stellar disc. An illustration of such phase functions, which take into account the finite dimension of the source of light, is depicted in Fig. 3 for WASP103b. For this example we assumed a stellar radius of $R^* = 1.44\,\mathrm{R}_\odot$ and a planet-to-star separation of $r \approx 4.27\,\mathrm{R}_\odot$ (Gillon et al. 2014; Southworth et al. 2015). The quadratic limb darkening coefficients $u_1 = 0.36$, $u_2 = 0.31$ were taken from Magic et al. (2015). This results in an angular radius of the stellar disc of WASP103 of 19.7 deg i.e. the whole star would appear on the planet's sky spanning almost 40 deg in diameter! One can see that the finite dimension of the source of light is important for larger particles or shorter wavelengths, but has almost no effect for smaller particles and/or longer wavelength. The FORTRAN90 code which reads our phase function tables and calculates such disc-averaged phase functions P_DA is provided together with the tables. As mentioned above, this code and pre-calculated P_DA phase functions are mainly useful in the case that a dust grain 'sees' a distinct source of light and/or in the optically thin dust regime. However, they might be utilized also within the planetary atmospheres, in which case, one could use P_DA for the first scattering event and $\overline{p}$ for subsequent scattering events in, e.g., Monte Carlo radiative transfer simulations.

4.3 Albedos

We calculate and tabulate both the absorption and scattering opacity as a function of wavelength for each modal particle radius. These tables and quantities can be used easily to calculate the single scattering albedos, ϖ, for each wavelength and modal particle radius via the expression

$$\varpi_\nu = \frac{\sigma_\nu^{\rm dust}}{\kappa_\nu^{\rm dust} + \sigma_\nu^{\rm dust}}. \quad (23)$$

If not mentioned otherwise, in the text below, by albedo we mean the single scattering albedo.

4.4 Grain equilibrium temperatures

Electromagnetic interaction with a particle results in heating that is ruled by the imaginary part of the complex refractive index $m_{\rm i}$ of the particle. The larger the $m_{\rm i}$, the more light (or electromagnetic radiation) is absorbed and consequently transformed to other forms of energy – most typically heat. Let us assume that a particle with an absorption cross-section $C_{\rm a}$ is irradiated by a radiation field with an intensity I_ν. The energy absorbed by the particle per unit time is

$$\frac{{\rm d}E^+}{{\rm d}t} = \iint C_{\rm a} I_\nu {\rm d}\omega {\rm d}\nu = 4\pi \int C_{\rm a} J_\nu {\rm d}\nu, \quad (24)$$

where ω is solid angle. Only angle subtended by the source (star) count since I_ν is zero elsewhere. J_ν is the mean intensity given by equation (20). We will assume that this energy is balanced by the thermal radiation of the particle at a rate

$$\frac{{\rm d}E^-}{{\rm d}t} = 4\pi \int C_{\rm a} B_\nu(T) {\rm d}\nu, \quad (25)$$

where $B_\nu(T)$ is the Planck function and T is the temperature of the grain. Multiplying both equations by the particle size distribution, integrating over the particle size, and dividing by 4π one recovers the radiative equilibrium equation in terms of opacities:

$$\int \kappa_\nu^{\rm dust} J_\nu {\rm d}\nu = \int \kappa_\nu^{\rm dust} B_\nu(T) {\rm d}\nu. \quad (26)$$

It is common practice to assume a blackbody radiation for the star and neglect its limb darkening, in which case the mean intensity can be expressed as

$$J_\nu = \frac{\omega}{4\pi} B_\nu(T^*). \quad (27)$$

In the above expression, T^* is the effective temperature of the star and ω is the solid angle subtended by the star:

$$\omega = 2\pi \left(1 - \sqrt{1 - \frac{R_\star^2}{d^2}}\right), \quad (28)$$

where $R_\star$ is radius of the star and d is the distance to the star centre. However, radiation emerging from stars or brown dwarfs may have significant departures from the blackbody radiation, especially in cooler objects with strong molecular and dust opacities. Brown dwarf spectra are dominated by the IR water bands which affect their SED, redistribute the flux towards shorter wavelengths, and interfere with our dust absorption. That is why, in the calculations of the left-hand side of equation (26), we use the fluxes, F_ν, from the model atmospheres rather than the Planck function. In this case, the following equation provides a much better estimate of the mean intensity (recall equation 2):

$$J_\nu = \frac{\omega}{4\pi} \frac{F_\nu(T^*)}{\pi}. \quad (29)$$

Equation (26) can be solved iteratively to obtain the grain temperature as a function of stellar temperature and solid angle. Numerical integration of the equations was performed using a simple trapezoidal rule. Particles of different sizes will have different temperatures as a result of their different absorption opacities. However, since our particle size distribution is relatively narrow, we assume that particles within the same distribution have the same temperature. Consequently, we calculate and tabulate grain temperatures only as a function of the modal radius of particles. Note that these are equilibrium temperatures an isolated grain would have, if there were no evaporation or grain growth. In reality, most of the grains will not survive at temperatures higher than the condensation temperature and will quickly evaporate (Kimura et al. 2002). Also, if gas is present, as e.g. in dense brown dwarf atmospheres, grains will exchange heat with the gas and both constituents settle to the same temperature (Woitke & Helling 2003). At much lower densities and in the presence of additional heating sources, like e.g. in protoplanetary disc atmospheres, condensates may have considerably cooler temperature than the ambient gas (Glassgold, Najita & Igea 2004).

Our grain temperatures cover a broad range of distances (solid angles). They decline with solid angle. This behaviour is not very interesting and, therefore to reveal other more interesting features, it is convenient to plot the grain temperatures relative to the temperature of the grey particle, $T^{\rm grey}$. The cross-section of grey particle does not depend on the frequency. In such case equation (26) gives

$$T^{\rm grey} = T^* \left(\frac{\omega}{4\pi}\right)^{1/4}. \quad (30)$$

This quantity will be used below to normalize and visualize the grain temperatures.

4.5 Radiative accelerations

Our tables can also be used to calculate the radiative acceleration $a_{\rm R}$ on a particle of certain modal radius and an average mass $\overline{M^{\rm g}}$. The radial component of the acceleration is

$$a_{\rm R} = \frac{1}{\overline{M^{\rm g}} c} \iint \overline{C_{\rm pr}} I_\nu {\rm d}\omega {\rm d}\nu, \quad (31)$$

where c is the speed of light and $\overline{C_{\rm pr}}$ is an averaged cross-section for radial component of the acceleration given by

$$\overline{C_{\rm pr}} = \int [C_{\rm a} A_1 + C_{\rm s} A_1 - \int \frac{p(\alpha)}{4\pi} C_{\rm s} A_0 {\rm d}\omega'] \frac{n_r}{n} {\rm d}r, \quad (32)$$

$A_1 = \cos\alpha_1, A_0 = \cos\alpha_0$, α_1 and α_0 are angles of the incoming and scattered rays with respect to the radial direction, respectively, α is the phase angle of the scattered beam (see Fig. 2). The integration is performed over all possible directions of the scattered photons ${\rm d}\omega'$, over all particle sizes ${\rm d}r$, over all directions of incidence ${\rm d}\omega$ with intensity I_ν, and over all frequencies. The first term is the contribution from absorption, which is angle independent since the thermal re-emission of the absorbed radiation is isotropic. The second and third terms contain the contribution from the scattered photons. Even for close-in planets, like WASP103b, one can assume a point source approximation and that $\cos\alpha_1 \approx 1$, $\cos\alpha_0 = \cos\alpha$. Using equations (4), (14), and (15) the following expression is obtained:

$$\overline{C_{\rm pr}} = \overline{C_{\rm a}} + (1-g)\overline{C_{\rm s}}. \quad (33)$$

Using the above formula and equations (20) and (27) one gets the following expression for the radiative acceleration:

$$a_{\rm R} = \frac{\omega}{\overline{M^{\rm g}} c} \int [\overline{C_{\rm a}} + (1-g)\overline{C_{\rm s}}] B_\nu(T^*) {\rm d}\nu \quad (34)$$

for the blackbody approximation, or

$$a_{\rm R} = \frac{\omega}{\overline{M^{\rm g}}\pi c}\int [\overline{C_{\rm a}} + (1-g)\overline{C_{\rm s}}]F_\nu(T^*){\rm d}\nu \quad (35)$$

when more precise fluxes, F_ν, on the surface of the source are known. This can be expressed in terms of opacities using equations (10) and (11):

$$a_{\rm R} = \frac{\omega}{\pi c}\int [\kappa^{\rm dust}_{\nu,\rho} + (1-g)\sigma^{\rm dust}_{\nu,\rho}]F_\nu(T^*){\rm d}\nu. \quad (36)$$

It is very convenient to express the radiative acceleration as $\beta = a_{\rm R}/a_{\rm G}$, i.e. relative to the gravitational acceleration:

$$a_{\rm G} = \frac{GM_*}{d^2}. \quad (37)$$

Combining equations (36), (37) and eliminating d using $\omega = \pi R_*^2/d^2$ one gets

$$\beta = \frac{R_*^2}{GM_*c}\int [\kappa^{\rm dust}_{\nu,\rho} + (1-g)\sigma^{\rm dust}_{\nu,\rho}]F_\nu(T^*){\rm d}\nu. \quad (38)$$

This β is now independent on the distance or ω. In this way we can calculate and tabulate β on the same grid of stellar effective temperatures T^* and particle sizes. We assumed $M_* = {\rm M}_\odot$, $R_* = {\rm R}_\odot$ and the user will need to adjust our β to his object $\beta_{\rm u}$, using the following relation:

$$\beta_{\rm u} = \beta\frac{R_*^2\,{\rm M}_\odot}{{\rm R}_\odot^2 M_*}. \quad (39)$$

The numerical integration of the equations was performed using a simple trapezoidal rule, as discussed next.

4.6 Numerical methods and precision

The numerical integration of the equations was performed using a simple trapezoidal rule on generally non-equidistant data points. To assess the robustness of the calculations we carried out a number of tests. First, we increased the number of integration points in the particle size distribution by a factor of 2. The opacities changed by less than 0.1 per cent, and the asymmetry parameter by 0.0002. Secondly, we extended the small size cut-off radius of the particle size distribution by a factor of 2. The opacities changed by less than 0.2 per cent, and the asymmetry parameter by less than 0.0004. Further, we extended the upper limit of the particle size distribution by a factor of 2 to larger particles. This is quite an important parameter. It resulted in the maximum change in the opacity of about 0.3 per cent and in the asymmetry parameter of about 0.0003. The scattering opacity is generally much more sensitive to this upper cut-off than the absorption opacity since, in the Rayleigh scattering regime, it increases with the cube of the particle radius. However, the absorption opacity may dominate such 'relative (fractional)' differences for case of transparent dust particles with a very low imaginary part of the refractive index and low absolute values of absorption opacities.

We also increased the angular resolution (decreased the integration step) in the calculations of phase functions by a factor of 2. The asymmetry parameter changed by less than 0.0005 for most of the particle sizes and wavelengths and the largest differences in g-values reached about 0.004.

When extracting fluxes from the model atmosphere tables we make a simple test and numerically calculate the integral of the whole SED: $\int F_\nu {\rm d}\nu$. This usually gives a small departure from the theoretical value of $\sigma T_{\rm eff}^4$. Then, we rescale the fluxes to match precisely the theoretical value. Consequently, we use the same integration pattern to calculate the dust temperatures and accelerations.

Our dust opacities have a short wavelength cut-off at 0.2 μm. For the purpose of calculating the radiative accelerations and dust temperatures, we extrapolate them with constant boundary value to 0.001 μm. If we were to cut them at 0.2 μm this would influence mainly the hottest stars, that radiate more at shorter wavelengths, and smaller grains that may have significant opacity increase at those wavelengths. We found out that the 0.2 μm cut-off did not change the radiative accelerations of 0.01 and 100 μm grains, irradiated by the $T_{\rm eff} = 7000$ K star, by more than 11 and 1 per cent, respectively, and is negligible for cooler models. Similarly, our dust opacities have a long wavelength cut-off at about 200–500 μm. We have also checked that neglecting the opacity at larger wavelengths has a negligible effect on the radiative accelerations, since our objects do not have a significant flux at those wavelengths.

However, this long wavelength opacity cut-off may not be negligible in the calculations of the dust temperatures. If the dust temperatures are low, the integral on the right-hand side of equation (26) may be underestimated causing artificially high dust temperatures. For a 500 μm cut-off, all grain temperatures that are less than about 30 K will be uncertain by more than 2–3 per cent. For ammonia and iron, which have about 200 μm opacity cut-off, such uncertainty is already noticeable at dust temperatures which are less than about 60 K.

5 OUTPUT – DESCRIPTION OF TABLES

We present our calculations in the form of four separate files for each dust species.

The first file, named e.g. iron_opac_all, deals with opacities. It contains blocks (separated by a blank line) and columns. Each block refers to a particular modal particle radius $r_{\rm c}$. It has five columns: (1) $\log(r_{\rm c})$ in μm, (2) wavelength in μm, (3) scattering opacity and (4) absorption opacity in cm^2/g (per gram means per gram of iron condensates), and (5) the mean cosine of the phase function.

The second file, named e.g. iron_phase_all, deals with phase functions. It contains several blocks, each block starts with $\log(r_{\rm c})$ in μm and refers to a particular modal radius. Each block has several sub-blocks, which apply to a given frequency and are preceded with its value in Hz, the mean cosine value, scattering and absorption opacities in cm^2/g (per gram means per gram of particular condensates). Each sub-block has two columns: phase angle in degrees and phase function normalized to 4π.

The third file, named e.g. iron_temp, deals with equilibrium temperatures. It also contains several blocks. Each block refers to a particular temperature of the star and modal particle radius. There are four columns: stellar effective temperature [K], $\log(r_{\rm c})$ in μm, solid angle subtended by the star in steradians, and grain equilibrium temperature [K].

The fourth file, named e.g. iron_radacc, contains radiative to gravitational acceleration ratio, β, (third column, dimensionless) as a function of the particle size [$\log(r_{\rm c})$ in μm, second column] and the stellar effective temperature (in K, first column). It assumes that the mass and radius of the irradiating object are ${\rm M}_\odot, {\rm R}_\odot$, respectively.

Opacities were to 0 and the phase functions to 1 in the wavelength regions where the refraction index measurements were not available. The provided 'readme' file contains the description of the tables and references to the original refractive index measurements of individual species. There is also a computer code DISKAVER.F90 in FORTRAN90 which calculates the disc-averaged phase functions.

The behaviour of the phase function, opacity, mean cosine, albedo, grain equilibrium temperature, and β is captured in Figs A1–A14.

The dust phase function is plotted using logarithmic scale for 1 μm particles. These phase functions indeed exhibit strong departures from isotropic scattering with very pronounced forward scattering peak. For large particles, this feature is proportional to the cross-section and rapidly increases with the square of the particle size. Towards low $x = 2\pi a/\lambda$ values (small particles and/or long wavelengths) forward scattering decreases and backward scattering increases, the phase functions approach the dipole phase function, $3(1 + \cos\alpha)/4$, and thus have a similar behaviour to Thomson or Rayleigh scattering (with some exceptions such as iron, see below). The asymmetry parameter reflects the behaviour of the phase functions.

Absorption and scattering opacities as well as the total opacity (absorption plus scattering) and albedo are also plotted using the logarithmic scale. Particles relatively small compared to the wavelength, with size parameter $x \ll 1$, (see e.g. chapter 5 of Bohren & Huffman 1983) show Rayleigh scattering pattern with the scattering efficiency proportional to $\sim x^4$. This results in a λ^{-4} wavelength dependence and a r^4 particle-size dependence. Consequently, the scattering cross-section is proportional to r^6 and the opacities per gram follow an r^3 dependence on particle size. If particles are large compared to the wavelength, i.e. $x \gg 1$, Q_e approaches a value of about 2 and both absorption and scattering opacities become noticeable grey.

Albedos are generally high in the optical region. However, notice that small particles at longer wavelength are in the Rayleigh scattering regime, which is not very effective. As a result, the albedo in this parameter space drops by many orders of magnitude to about 10^{-10}. In the figures, we deliberately saturate this regime and assign a dark brown colour to albedos smaller than 10^{-4}. The grain temperatures decrease with decreasing solid angle. For this reason they are plotted relatively to the grey temperatures, $T/T^{\rm grey}$, (see equation 30) for a solar type star with $T^\star = 5800$ K on a grid of modal particle sizes and solid angles. As the opacities of most large particles become progressively more grey, this results in more grey albedos and equilibrium temperatures.

β values are plotted as a function of particle size for 13 star/brown dwarf temperatures (see Section 3). Generally, radiative accelerations can exceed gravity for hotter stars but the ratio decreases with decreasing object temperatures. The β values all show a pronounced peak at a certain particle size. Assuming a blackbody radiation of the object, this peak would be at lower grain radii for hotter stars and would move towards larger particles for cooler objects. This is due to predominant scattering and its λ^{-4} dependence for small particles together with strong fluxes at the shorter wavelengths for hot objects. In the cooler objects, the fluxes move to longer wavelengths and so does the Rayleigh regime for larger particles, and this enables larger particles to pick-up more momentum. We observe that this trend also holds for stars without the blackbody assumption, i.e. assuming synthetic spectra from atmospheric models. However, it stalls and may even get reversed in objects cooler than about 1600 K. This is associated with the L–T transition. In T-type brown dwarfs, the opaque silicate dust clouds settle into deeper layers, atmosphere clears, strong molecular absorption in the IR region pushes the flux via shorter wavelengths reversing the $J - K$ colour index. Generally, such 'non-blackbody' radiative accelerations of larger particles, that tend to have more grey opacities, do not differ much from the 'blackbody' accelerations, with the exception of water and ammonia. However, such 'non-blackbody' accelerations of 0.1–0.3 μm particles around cool L, T type objects may often be by a factor of 3–5 higher than their 'blackbody' counterparts. In the next section we briefly summarize the most striking features for different species, which may be used to identify that particular species in the spectra/photometry of exoplanets.

6 RESULTS

Alumina/corundum: (Figs A1 and A2) absorption opacities of smaller particles show a strong 12 μm peak (Koike et al. 1995; Zeidler et al. 2013) which turns into a depression for larger particles (Koike et al. 1995; Zeidler et al. 2013). Scattering shows a dip at 8–9 μm, a peak at 12 μm for smaller particles, and a relatively flat behaviour for larger particles. As a consequence we see a strong 12 μm feature in the total opacity of small particles but an enhanced albedo in the 10–30 μm region for larger particles. This is accompanied by a sharp drop in the mean cosine of the scattering angle g at about 10 μm for larger particles. Overall g is positive and approaches unity for larger particles and $\lambda < 10$ μm. One can see strong forward scattering but weak backward scattering features. Alumina has moderate absorption in the optical regime and its equilibrium temperatures approach that of the grey absorber. Smaller particles, when irradiated by a solar type star with solid angle 10^{-1}–10^{-3}, tend to have about 50 per cent higher temperatures than the grey absorber. Large crystallized corundum particles are quite reflective and have higher albedo in the IR–far-IR regime than γ alumina.

Perovskite: (Fig. A3) has a strong absorption feature at 14.1 μm and weaker features at 21.0, 23.8, 33, and 62.3 μm (Posch et al. 2003). Its albedo is very high in the near-IR region and remains so for large particles also at the longer wavelengths. Significant drops in the albedo are observed near the above-mentioned absorption features. Mean cosine of the phase function reaches negative values at longer wavelengths and for larger particles which indicates significant back-scattering properties. On the other hand, highly positive peak g-values are found at 11 and 20 μm for large particles.

Forsterite: (Fig. A4) absorption opacities of forsterite show the typical double peak at 10 and 18 μm, which is due to stretching and bending of Si–O molecular bond in silicates. Scattering opacities generally dominate in the visible region and become progressively more important at longer wavelengths as the particle size increases. Smaller grain sizes exhibit the λ^{-4} dependence typical of the Rayleigh regime. These opacity properties are well known and we will now focus on the behaviour of the phase functions. The mean cosine of the scattering angle is positive, which indicates predominance of the forward scattering. Forward and backward scattering increase towards shorter wavelengths or larger particles. As the particle size increases backward scattering first disappears at shorter wavelength and then re-emerges and expands to progressively longer wavelength. Phase functions also show strong wavelength dependence in the vicinity of 10–18 μm features. Forsterite absorbs little flux in the optical region which results in its equilibrium temperatures for solar type stars being significantly lower than those of the grey absorber. Its albedo is very close to unity in the optical and NIR regions but large particles remain reflective also in the far-IR and sub-mm region. Broad absorption bands at 10–20 μm significantly reduce its albedo.

Olivine: (Fig. A5) with 50 per cent of iron has considerably stronger absorption in UV, visible, and NIR region than forsterite for smaller and medium size particles. Small olivine particles have

slightly higher total opacity in the NIR region. The 10 μm feature is sharper, especially its blue edge, while the 20 μm feature is slightly broader. The albedo of olivine is significantly smaller than that of forsterite in the whole optical and NIR region. Consequently, the equilibrium grain temperatures of medium to small particles are several times higher than those of forsterite. Larger olivine particles have temperatures similar to the grey particles. This is a consequence of the imaginary part of the refractive index of olivine, which is much higher in the optical and NIR regions. Radiative accelerations of the small olivine particles are significantly higher than those of forsterite and the maximum is less pronounced. The forward scattering of 1 μm particles in the optical region is narrower while back-scattering peak diminished and, consequently, the asymmetry parameter of medium size grains is larger.

Enstatite: (Fig. A6) behaves in a similar way as forsterite. Its absorption opacity in the visible and near-IR regions is small, even smaller than that of forsterite. Consequently, its equilibrium temperatures are considerably below the grey absorber and even lower than those of forsterite. The phase functions and mean cosine of the phase angle show even more pronounced wavelength dependence in the 4–20 μm region. The albedo of enstatite has similar behaviour to that of forsterite. Both iron-free silicates, forsterite, and enstatite, show a pronounced peak in β values with relatively low radiative accelerations, especially for small grains, when compared to other species.

Pyroxenes: (Figs A7 and A8) even a small amount of iron considerably raises the imaginary part of the refractive index in the UV, visible, and near-IR regions (Dorschner et al. 1995). This raises the absorption opacity and equilibrium grain temperatures. Particularly small grains, at relatively close distance to a solar type star, with a 20 per cent amount of iron, may become almost two times hotter relative to the grey absorber. Larger particles can still remain relatively cool at larger distances. Its albedo shows similarities to iron-free silicates but we start to see an enhanced absorption in the UV for larger particles and accompanied reduction of the albedo. This trend gets even more pronounced and spreads to longer wavelengths and smaller particles if the amount of iron is increased to 60 per cent. The presence of iron has also an effect on the phase functions and increases the mean cosine of the scattering angle for $\lambda < 4$ μm. Backward scattering is apparent in visible and near-IR regions; however, it diminishes for large particles in UV region and this trend is more pronounced with higher iron content.

Iron: (Fig. A9) contrary to silicates, iron has considerable absorption opacity in the visible and IR, which generally smoothly declines towards longer wavelengths and larger particles. Its absorption and scattering opacities are almost featureless (grey) apart from the Rayleigh scattering regime for smaller particles. The mean cosine of the scattering angle increases with the particle size and towards shorter wavelengths. It may have significant negative values, especially at longer wavelengths, which is due to a very pronounced backward scattering peak. For larger particles, forward scattering overcomes the backward scattering at shorter and progressively at longer wavelengths. These features can be used to identify iron in exoplanets. Highly effective absorption properties in the optical and IR regions heat iron grains to significantly higher temperatures as expected for the grey absorber. Especially, small iron grains at large distances from solar-type stars can get heated to temperatures more than a factor of 3 higher than the grey absorber. As a result of its opacity behaviour, large iron particles are efficient at scattering in the IR and far-IR regime. However, compared to silicates, iron particles (especially small ones) have quite low albedo in the UV and visible regions. β values peak at slightly smaller grains than most of other species. Small iron grains will acquire significantly higher radiative accelerations than other species when irradiated by stars. This is due to high iron opacities in the optical as well as strong back-scattering properties which push the particles away from the source. On the contrary, larger iron grains tend to have slightly smaller β values for all source temperatures.

Carbon: (Figs A10 and A11) differs from most of the species but some features resemble those of pure iron. Carbon at higher temperatures and higher graphitization, has a total opacity which smoothly declines towards longer wavelengths and larger particles. Apart from the slope, the dominant 'feature' is the fact that it is almost featureless. There is a drop in the absorption and scattering opacities of small particles in the UV. The most striking characteristic is that its albedo in the optical and IR regions is much smaller than that of other species, even smaller than that of iron. However, the albedo of large particles at far-IR and sub-mm wavelengths is approaching unity. The asymmetry parameter is mostly positive and smoothly increases towards the shorter wavelength. However, it becomes negative for larger particles in the sub-mm region, a feature indicating stronger backward scattering but not as pronounced as in iron. The phase functions lack any abrupt features too.

Carbon at cooler temperatures has a steeper gradient of the total opacity in the IR region but more shallow in the far-IR and sub-mm region (Jager et al. 1998). Its albedo features an enhanced band travelling from medium size particles at NIR region towards larger particles at sub-mm region caused by an enhanced scattering at the blue edge of the Rayleigh scattering regime. Apart from this feature, the opacities are almost perfectly grey and featureless. Contrary to its behaviour at hotter temperatures, the asymmetry parameter is everywhere positive and increasing smoothly towards larger particles and shorter wavelengths. Dust temperatures of larger particles and closer to the solar type star are slightly cooler while smaller particles which are farther from the star are significantly hotter than the grey absorber. Small carbon grains acquire the highest radiative accelerations of all the species studied here.

Water ice: (Fig. A12) absorbs very little in the visible but has strong absorption and scattering features in the IR, particularly at about 3 μm, and shallower features at about 12 and 40–50 μm. This is accompanied by the variability of phase functions at these wavelengths. Mean cosine values of larger particles show extra particle size sensitivity in the 3–10 μm region and is larger than zero. However, broad back-scattering feature is present in the visible region. Its extremely low absorption in the optical causes the grains to be significantly cooler than those of the grey absorber for hotter stars. Its high absorption in the IR, however, might heat smaller grains at large distances to become hotter than grey absorber when irradiated by cooler brown dwarfs. The albedo of water ice is very high, essentially 1, for all particles from UV to NIR. Large ice particles are slightly more reflective than liquid drops in the far-IR and sub-mm regimes. In the IR one can see the water absorption bands which lower its albedo.

Water liquid: (Fig. A13) has similar features as ice. It has slightly more pronounced absorption features, e.g. a nib at about 6 μm, and slightly higher UV and blue absorption. Mean cosine values of larger particles show enhanced particle size sensitivity in the 3–10 μm region.

Ammonia: (Fig. A14) has very sharp and strong absorption and scattering features at about 3, 9.4, 26, 70, 110–140 μm, which may interfere with the water and silicate features. Its absorption in the visible is much stronger than that of water. Apart from forward scattering, its phase functions exhibit also back scattering at the shorter wavelengths and strong variability with wavelength

at the above-mentioned spectral regions which can help to identify ammonia in reflected light. The equilibrium grain temperatures of ammonia are similar to those of water but larger particles tend to follow the trend of the grey absorber while smaller particles at medium distances are even cooler. Overall, the albedo of ammonia has similar characteristics as that of water ice. A number of absorption features can be seen which reduce its albedo in the IR and far-IR regions. Medium to large ammonia grains also experience strong radiative push compared to other particles.

7 CONCLUSIONS

We have calculated phase functions, asymmetry parameters, absorption and scattering opacities, single scattering albedos, equilibrium dust grain temperatures, and radiative accelerations for about a dozen of the species most commonly encountered in the extrasolar planet environment. Mie theory and spherical homogeneous grains are assumed. The optical properties are integrated across a poly-dispersed Deirmendjian particle size distribution with different modal particle radii. These distributions are relatively narrow. Consequently, they might be understood as single-sized particles with the radius equal to the modal radius or used to assemble and study an optional broader particle size distribution, if necessary. These dust properties are presented in the form of tables as a function of wavelength and modal particle size. Equilibrium grain temperatures are a function of modal particle size, host star effective temperature, and solid angle subtended by the star. Radiative accelerations are tabulated as a function of modal particle radius and host star temperatures. Dust opacities are deliberately calculated per gram of the dust material so that the user has more flexibility and can place these dust particles into any environment independently on the gas to dust ratio. Tables will be maintained, potentially expanded, and available for download from http://www.ta3.sk/∼budaj/dust.

There is also a code which allows the user to take into account, an optional, finite dimension of the source of light (star) and calculate grid of disc-averaged phase functions.

ACKNOWLEDGEMENTS

The authors would like to thank Simon Zeidler and Harald Mutschke for valuable consultations about the optical data as well as Hannah Wakeford for comments about the manuscript. JB and RS acknowledge funding by the Australian Research Council Discovery Project Grant DP120101792. MK acknowledges support by the Slovak National Grant Agency VEGA grant no. 2/0002/12 and JB also acknowledges partial support by VEGA 2/0143/14.

REFERENCES

Ackerman A. S., Marley M. S., 2001, ApJ, 556, 872
Allard F., Hauschildt P. H., Alexander D. R., Tamanai A., Schweitzer A., 2001, ApJ, 556, 357
Allard F., Guillot T., Ludwig H.-G., Hauschildt P. H., Schweitzer A., Alexander D. R., Ferguson J. W., 2003, in Martín E., ed., Proc. IAU Symp. 211, Brown Dwarfs. Astron. Soc. Pac., San Francisco, p. 325
Asplund M., Grevesse N., Sauval A. J., Scott P., 2009, ARA&A, 47, 481
Baraffe I., Homeier D., Allard F., Chabrier G., 2015, A&A, 577, A42
Beichman C. et al., 2014, PASP, 126, 1134
Bochinski J. J., Haswell C. A., Marsh T. R., Dhillon V. S., Littlefair S. P., 2015, ApJ, 800, L21
Bohren C. F., Huffman D. R., 1983, Absorption and Scattering of Light by Small Particles. Wiley, New York
Broeg C. et al., 2013, in Saglia R., ed., EPJ Web Conf. Vol. 47, Hot Planets and Cool Stars. EDP Sciences, Garching, p. 3005
Brogi M., Keller C. U., de Juan Ovelar M., Kenworthy M. A., de Kok R. J., Min M., Snellen I. A. G., 2012, A&A, 545, L5
Budaj J., 2011, A&A, 532, L12
Budaj J., 2013, A&A, 557, A72
Burrows A., Sudarsky D., Hubeny I., 2006, ApJ, 640, 1063
Burrows A., Budaj J., Hubeny I., 2008, ApJ, 678, 1436
Caffau E., Ludwig H.-G., Steffen M., Freytag B., Bonifacio P., 2011, Sol. Phys., 268, 255
Cahoy K. L., Marley M. S., Fortney J. J., 2010, ApJ, 724, 189
Cowan N. B., Agol E., 2011, ApJ, 729, 54
Croll B. et al., 2014, ApJ, 786, 100
Cuzzi J. N., Estrada P. R., Davis S. S., 2014, ApJS, 210, 21
de Kok R. J., Stam D. M., 2012, Icarus, 221, 517
Deirmendjian D., 1964, Appl. Opt., 3, 187
Deming D. et al., 2009, PASP, 121, 952
Dong S. et al., 2014, ApJ, 788, 41
Dorschner J., Begemann B., Henning T., Jaeger C., Mutschke H., 1995, A&A, 300, 503
Ferraro J. R., Sill G., Fink U., 1980, Appl. Spectrosc., 34, 525
García Muñoz A., Pallé E., 2011, J. Quant. Spectrosc. Radiat. Transfer, 112, 1609
García Muñoz A., Pallé E., Zapatero Osorio M. R., Martín E. L., 2011, Geophys. Res. Lett., 38, 14805
Gardner J. P. et al., 2006, Space Sci. Rev., 123, 485
Gillon M. et al., 2014, A&A, 562, L3
Glassgold A. E., Najita J., Igea J., 2004, ApJ, 615, 972
Helling C. et al., 2008, MNRAS, 391, 1854
Heng K., Mendonça J. M., Lee J.-M., 2014, ApJS, 215, 4
Henning T., Il'In V. B., Krivova N. A., Michel B., Voshchinnikov N. V., 1999, A&AS, 136, 405
Howe A. R., Burrows A. S., 2012, ApJ, 756, 176
Hubeny I., Lanz T., 1995, ApJ, 439, 875
Hubeny I., Burrows A., Sudarsky D., 2003, ApJ, 594, 1011
Jager C., Mutschke H., Henning T., 1998, A&A, 332, 291
Jäger C., Il'in V. B., Henning T., Mutschke H., Fabian D., Semenov D., Voshchinnikov N., 2003a, J. Quant. Spectrosc. Radiat. Transfer, 79, 765
Jäger C., Dorschner J., Mutschke H., Posch T., Henning T., 2003b, A&A, 408, 193
Johnson P. B., Christy R. W., 1974, Phys. Rev. B, 9, 5056
Kane S. R., Gelino D. M., 2011, ApJ, 729, 74
Kimura H., Mann I., Biesecker D. A., Jessberger E. K., 2002, Icarus, 159, 529
Knutson H. A., Charbonneau D., Allen L. E., Burrows A., Megeath S. T., 2008, ApJ, 673, 526
Kocifaj M., 1994, Stud. Geophys. Geod., 38, 304
Kocifaj M., Horvath H., 2005, Appl. Opt., 44, 7378
Koike C., Kaito C., Yamamoto T., Shibai H., Kimura S., Suto H., 1995, Icarus, 114, 203
Kreidberg L. et al., 2014, Nature, 505, 69
Lee J.-M., Irwin P. G. J., Fletcher L. N., Heng K., Barstow J. K., 2014, ApJ, 789, 14
Lodders K., 2003, ApJ, 591, 1220
Lodders K., Fegley B., Jr, 2006, in Mason J. W., ed., Astrophysics Update 2. Praxis Publishing Ltd, Chichester, UK, p. 1
Madhusudhan N., Burrows A., 2012, ApJ, 747, 25
Madhusudhan N., Burrows A., Currie T., 2011, ApJ, 737, 34
Magic Z., Chiavassa A., Collet R., Asplund M., 2015, A&A, 573, A90
Marley M. S., Gelino C., Stephens D., Lunine J. I., Freedman R., 1999, ApJ, 513, 879
Marley M. S., Saumon D., Cushing M., Ackerman A. S., Fortney J. J., Freedman R., 2012, ApJ, 754, 135
Marley M. S., Ackerman A. S., Cuzzi J. N., Kitzmann D., 2013, in Mackwell S. J., Simon-Miller A. A., Harder J. W., Bullock M. A., eds, Comparative Climatology of Terrestrial Planets. Univ. Arizona Press, Tucson, AZ, p. 367
Martonchik J. V., Orton G. S., Appleby J. F., 1984, Appl. Opt., 23, 541

Meng Z., Quillen A. C., Bell C. P. M., Mamajek E. E., Scott E. L., Zhou J.-L., 2014, MNRAS, 441, 3733
Mordasini C., 2014, A&A, 572, A118
Morley C. V., Fortney J. J., Marley M. S., Visscher C., Saumon D., Leggett S. K., 2012, ApJ, 756, 172
Morley C. V., Fortney J. J., Kempton E. M.-R., Marley M. S., Visscher C., Zahnle K., 2013, ApJ, 775, 33
Morley C. V., Marley M. S., Fortney J. J., Lupu R., Saumon D., Greene T., Lodders K., 2014, ApJ, 787, 78
Ordal M. A., Bell R. J., Alexander R. W., Jr, Newquist L. A., Querry M. R., 1988, Appl. Opt., 27, 1203
Ormel C. W., 2014, ApJ, 789, L18
Pallé E., García Muñoz A., Zapatero Osorio M. R., Montañés-Rodríguez P., Barrena R., Martín E. L., 2011, in Sozzetti A., Lattanzi M. G., Boss A. P., eds, Proc. IAU Symp. 276, The Astrophysics of Planetary Systems: Formation, Structure, and Dynamical Evolution. Cambridge Univ. Press, Cambridge, p. 385
Pollack J. B., Hollenbach D., Beckwith S., Simonelli D. P., Roush T., Fong W., 1994, ApJ, 421, 615
Pont F., Sing D. K., Gibson N. P., Aigrain S., Henry G., Husnoo N., 2013, MNRAS, 432, 2917
Posch T., Kerschbaum F., Fabian D., Mutschke H., Dorschner J., Tamanai A., Henning T., 2003, ApJS, 149, 437
Rappaport S. et al., 2012, ApJ, 752, 1
Rappaport S., Barclay T., DeVore J., Rowe J., Sanchis-Ojeda R., Still M., 2014, ApJ, 784, 40
Rattenbury N. J. et al., 2015, MNRAS, 447, L31
Rauer H. et al., 2014, Exp. Astron., 38, 249
Ricker G. R. et al., 2014, in Oschmann J. M., Jr, Clampin M., Fazio G. G., MacEwen H. A., eds, Proc. SPIE Conf. Ser. Vol. 9143, Space Telescopes and Instrumentation 2014: Optical, Infrared, and Millimeter Wave. SPIE, Bellingham, p. 20
Rowe J. F. et al., 2008, ApJ, 689, 1345
Sánchez-Lavega A., Pérez-Hoyos S., Hueso R., 2004, Am. J. Phys., 72, 767
Sanchis-Ojeda R. et al., 2015, preprint (arXiv:1504.04379)
Satorre M. Á., Leliwa-Kopystynski J., Santonja C., Luna R., 2013, Icarus, 225, 703
Seager S., Whitney B. A., Sasselov D. D., 2000, ApJ, 540, 504
Segelstein D., 1981, M.S. thesis, Univ. Missouri-Kansas City
Sing D. K. et al., 2013, MNRAS, 436, 2956
Southworth J. et al., 2015, MNRAS, 447, 711
Stam D. M., 2008, A&A, 482, 989
Sudarsky D., Burrows A., Pinto P., 2000, ApJ, 538, 885
Sudarsky D., Burrows A., Hubeny I., Li A., 2005, ApJ, 627, 520
Tinetti G., Meadows V. S., Crisp D., Kiang N. Y., Kahn B. H., Fishbein E., Velusamy T., Turnbull M., 2006, Astrobiology, 6, 881
Tinetti G. et al., 2012, Exp. Astron., 34, 311
Tinetti G. et al., 2015, preprint (arXiv:1502.05747)
Tsuji T., 2002, ApJ, 575, 264
van Lieshout R., Min M., Dominik C., 2014, A&A, 572, A76
van Werkhoven T. I. M., Brogi M., Snellen I. A. G., Keller C. U., 2014, A&A, 561, A3
Wakeford H. R., Sing D. K., 2015, A&A, 573, A122
Warren S. G., Brandt R. E., 2008, J. Geophys. Res., 113, 14220
Woitke P., Helling C., 2003, A&A, 399, 297
Zeidler S., Posch T., Mutschke H., 2013, A&A, 553, A81

APPENDIX A

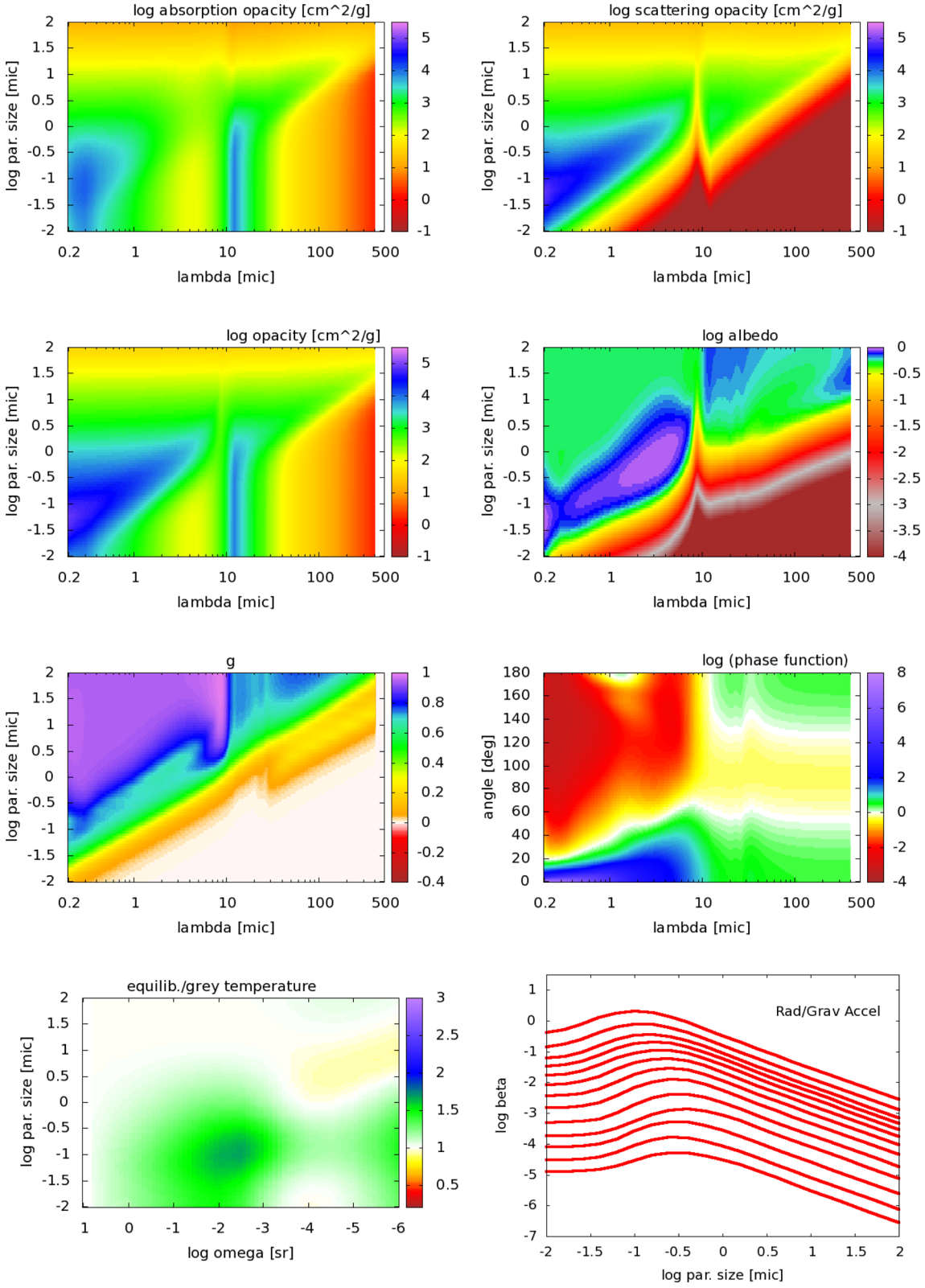

Figure A1. Alumina. Very top: absorption and scattering opacities. Top left: total opacity (scattering plus absorption). Top right: single scattering albedo. Middle left: mean cosine of the scattering angle. Middle right: phase function for modal particle radius of 1 μm. Bottom left: grain temperature relative to the grey absorber for a solar type star with $T^* = 5800$ K. Bottom right: radiative acceleration relative to the gravity of the central object for 13 stellar temperatures, from the top – 7000, 5800, 5000, 4500, 4000, 3500, 3000, 2500, 2000, 1600, 1200, 900, and 700 K.

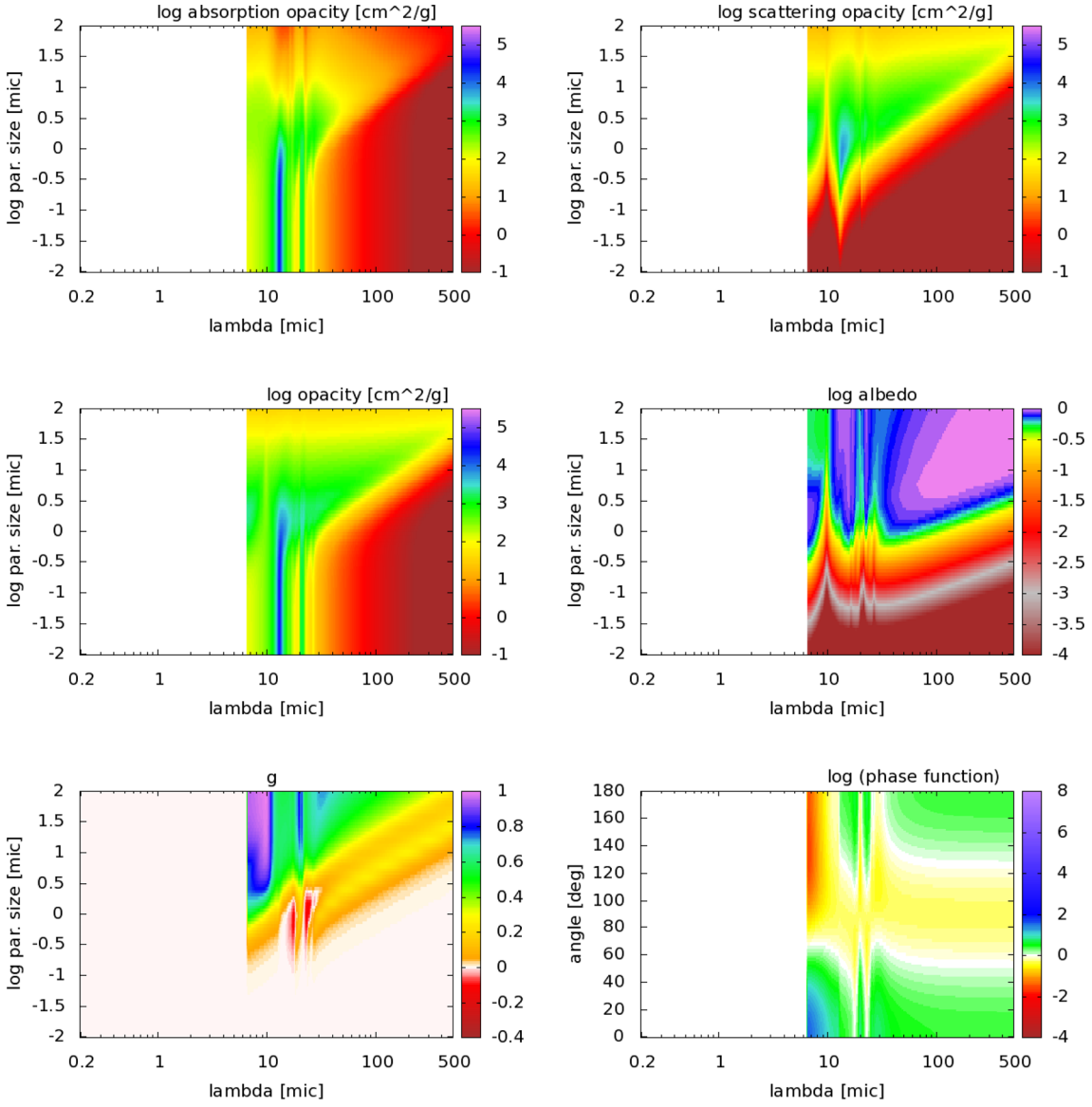

Figure A2. Corundum. Pictures and notation are the same as in the previous figure. Dust temperatures and accelerations are not calculated in this case because the opacities do not cover the whole spectral region.

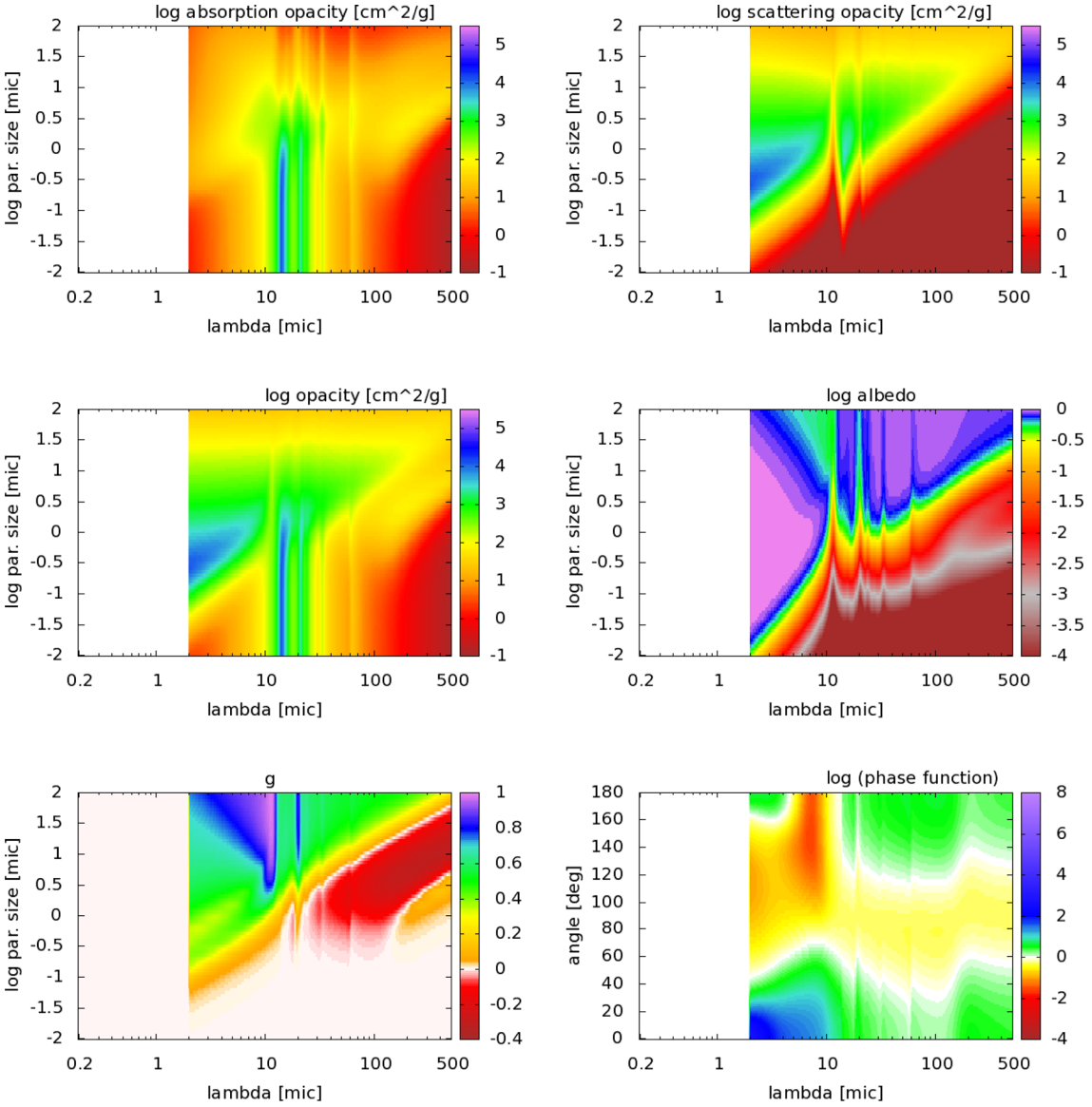

Figure A3. Perovskite. Pictures and notation are the same as in the previous figure. Dust temperatures and accelerations are not calculated in this case because the opacities do not cover the whole spectral region.

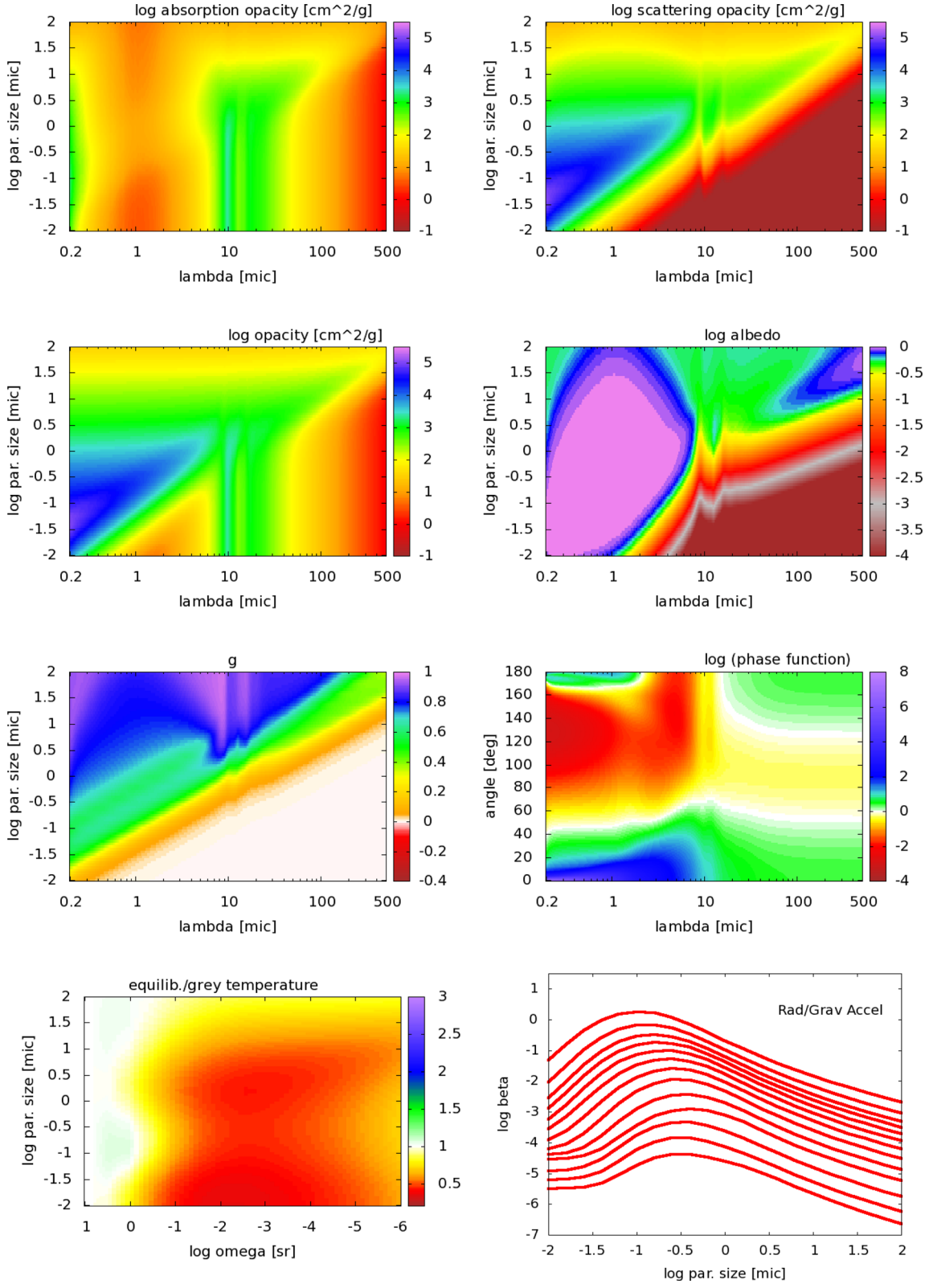

Figure A4. Forsterite. Pictures and notation are the same as in the previous figure.

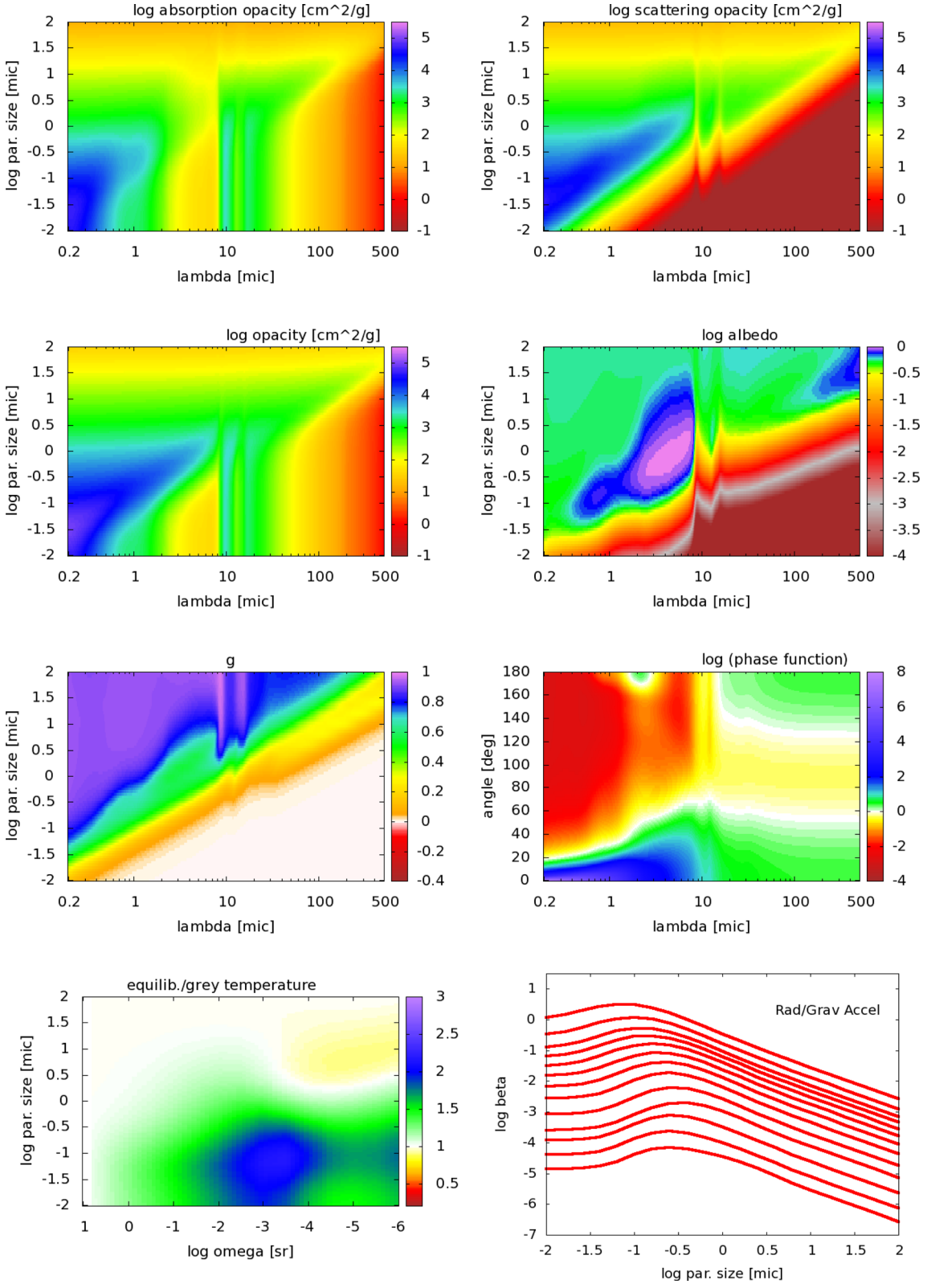

Figure A5. Olivine with 50 per cent of iron. Pictures and notation are the same as in the previous figure.

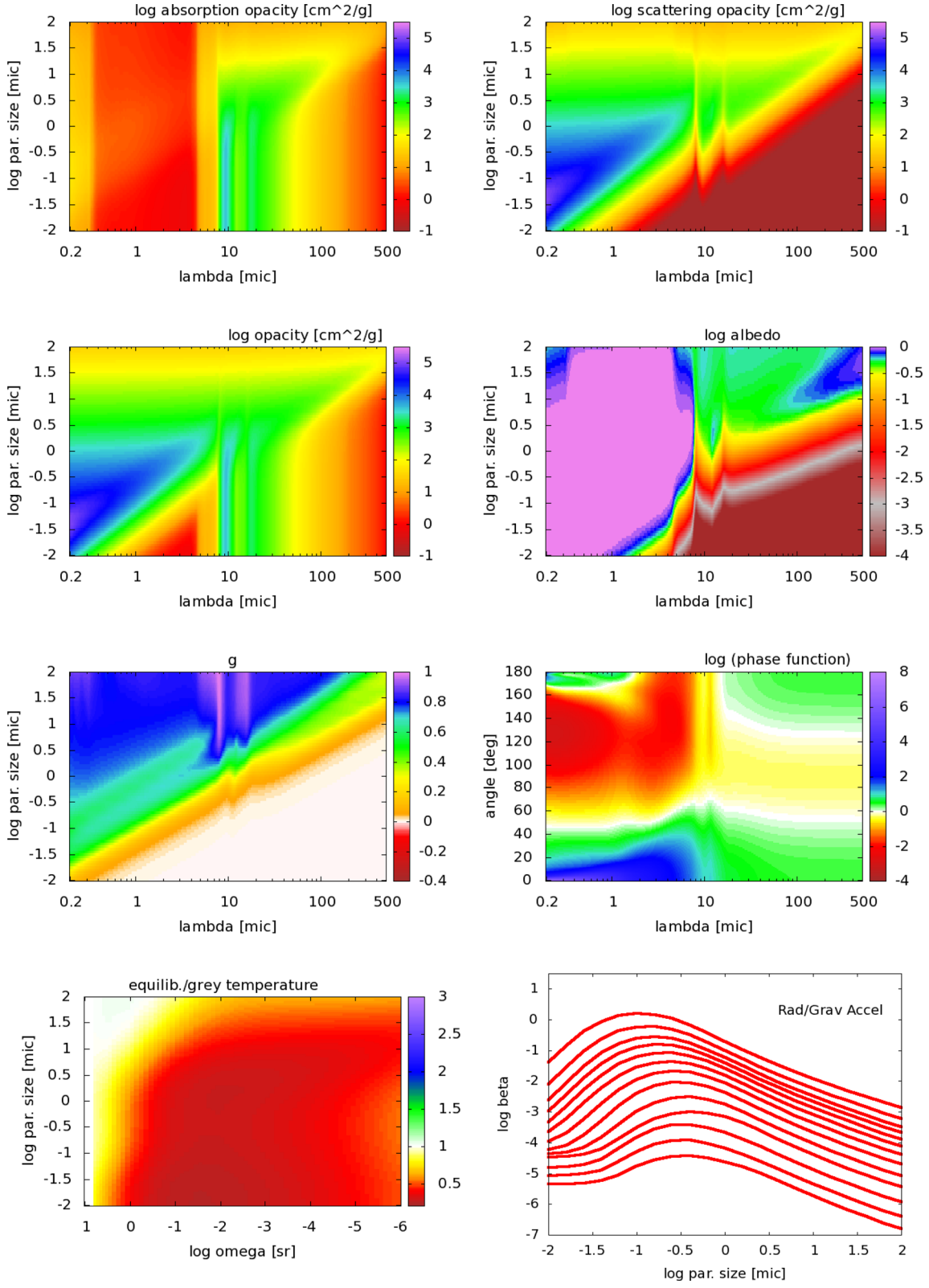

Figure A6. Enstatite. Pictures and notation are the same as in the previous figure.

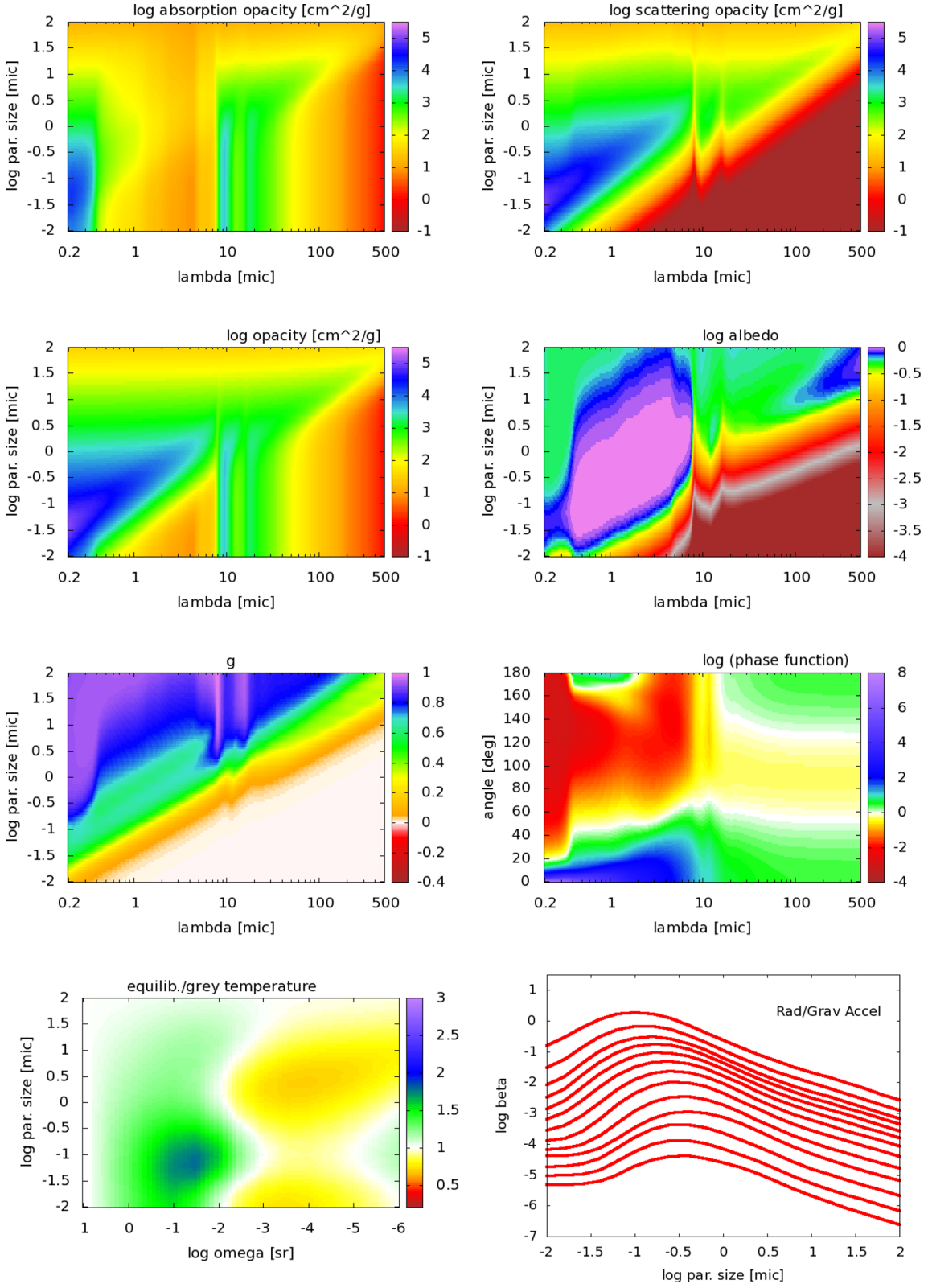

Figure A7. Pyroxene with 20 per cent or iron. Pictures and notation are the same as in the previous figure.

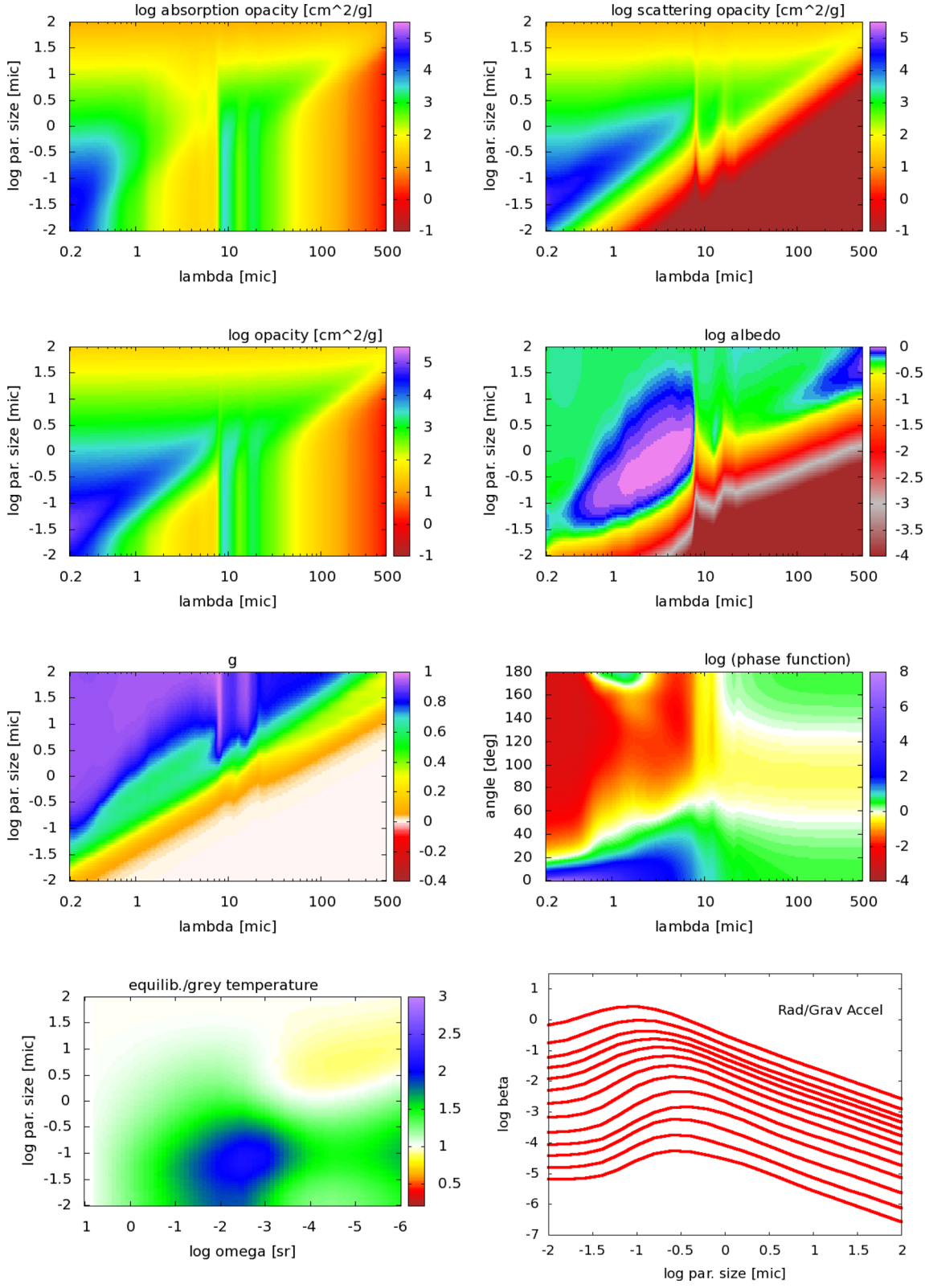

Figure A8. Pyroxene with 60 per cent or iron. Pictures and notation are the same as in the previous figure.

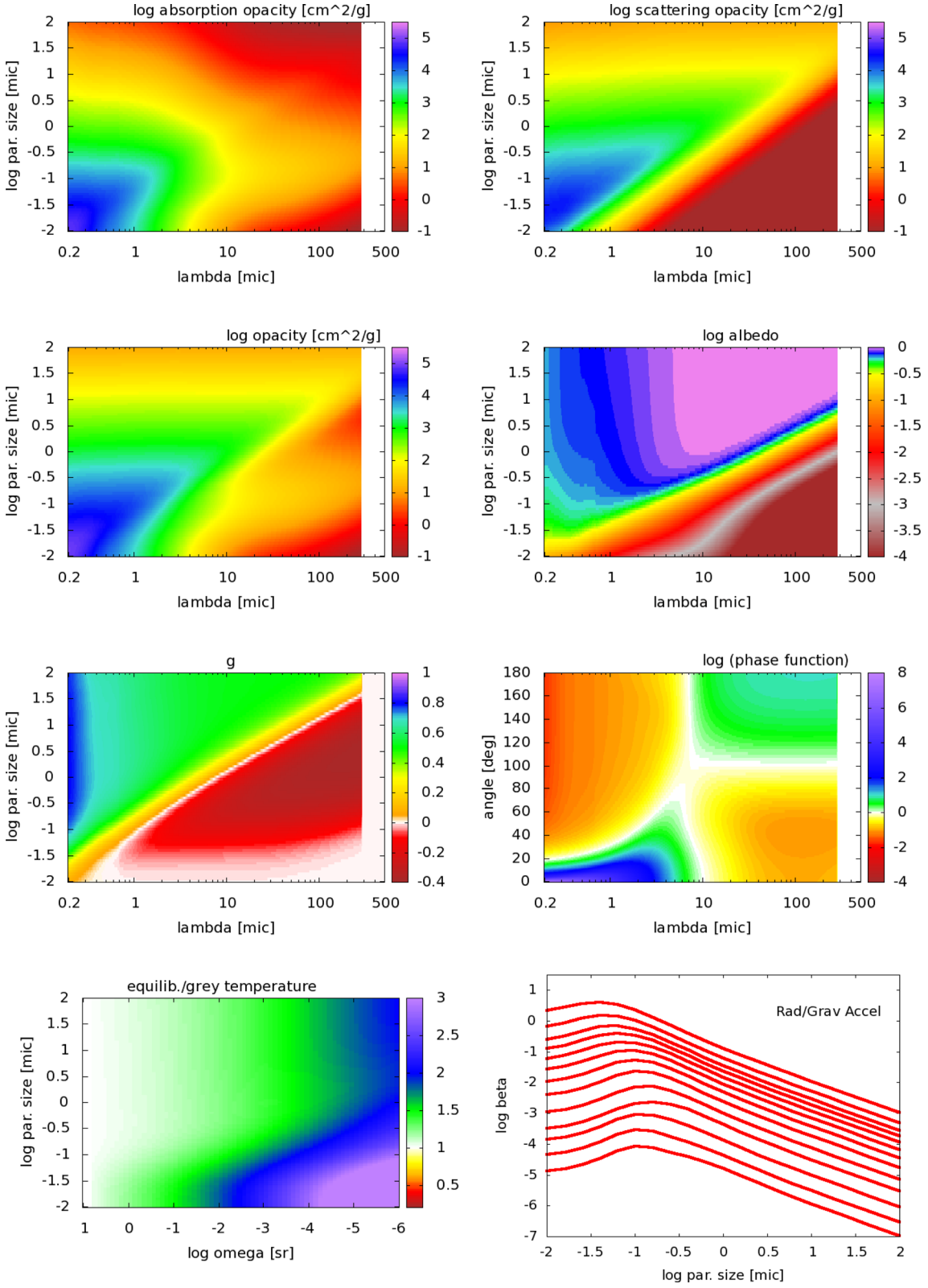

Figure A9. Iron. Pictures and notation are the same as in the previous figure.

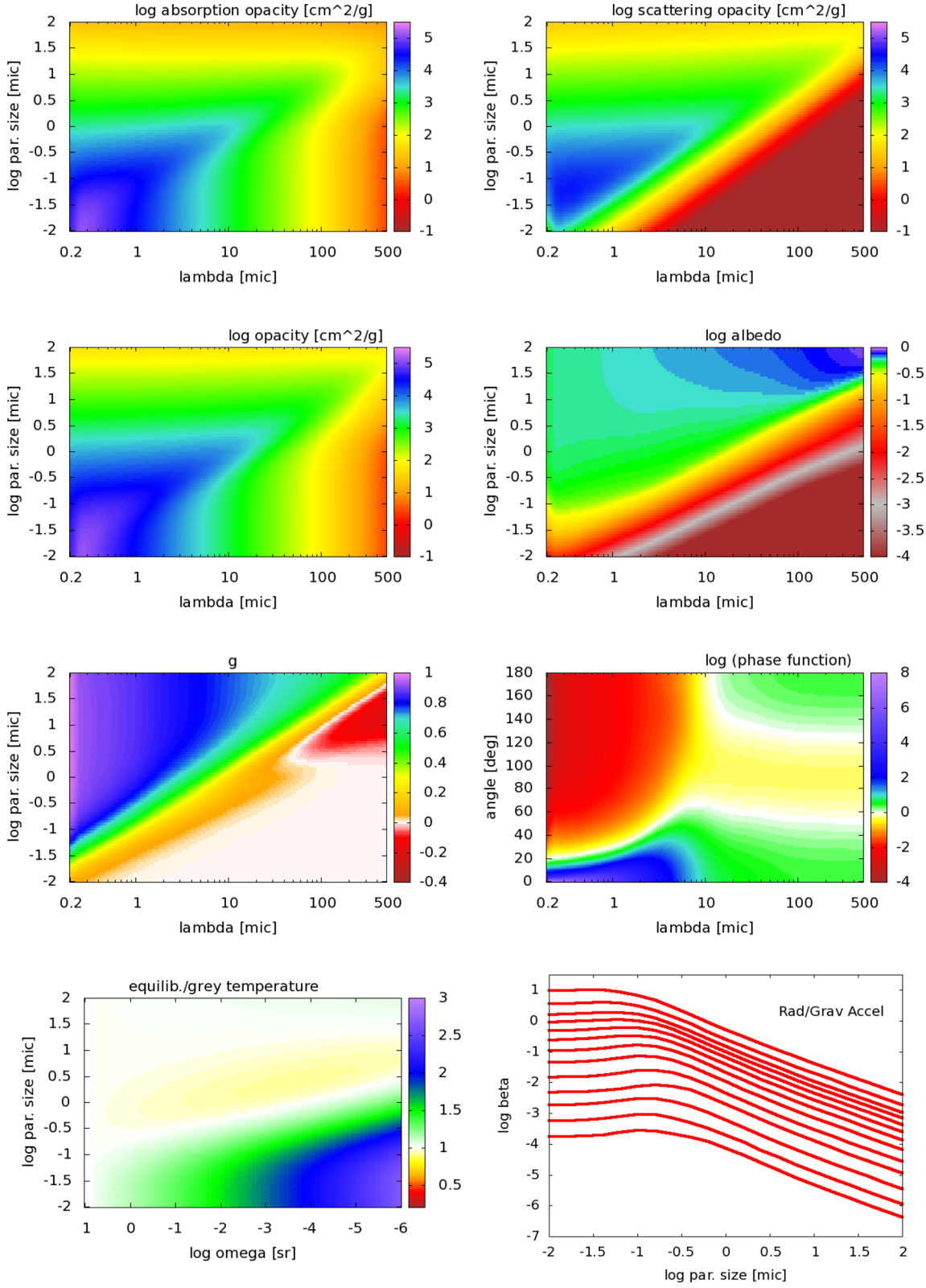

Figure A10. Carbon assuming optical data for 1000°C. Pictures and notation are the same as in the previous figure.

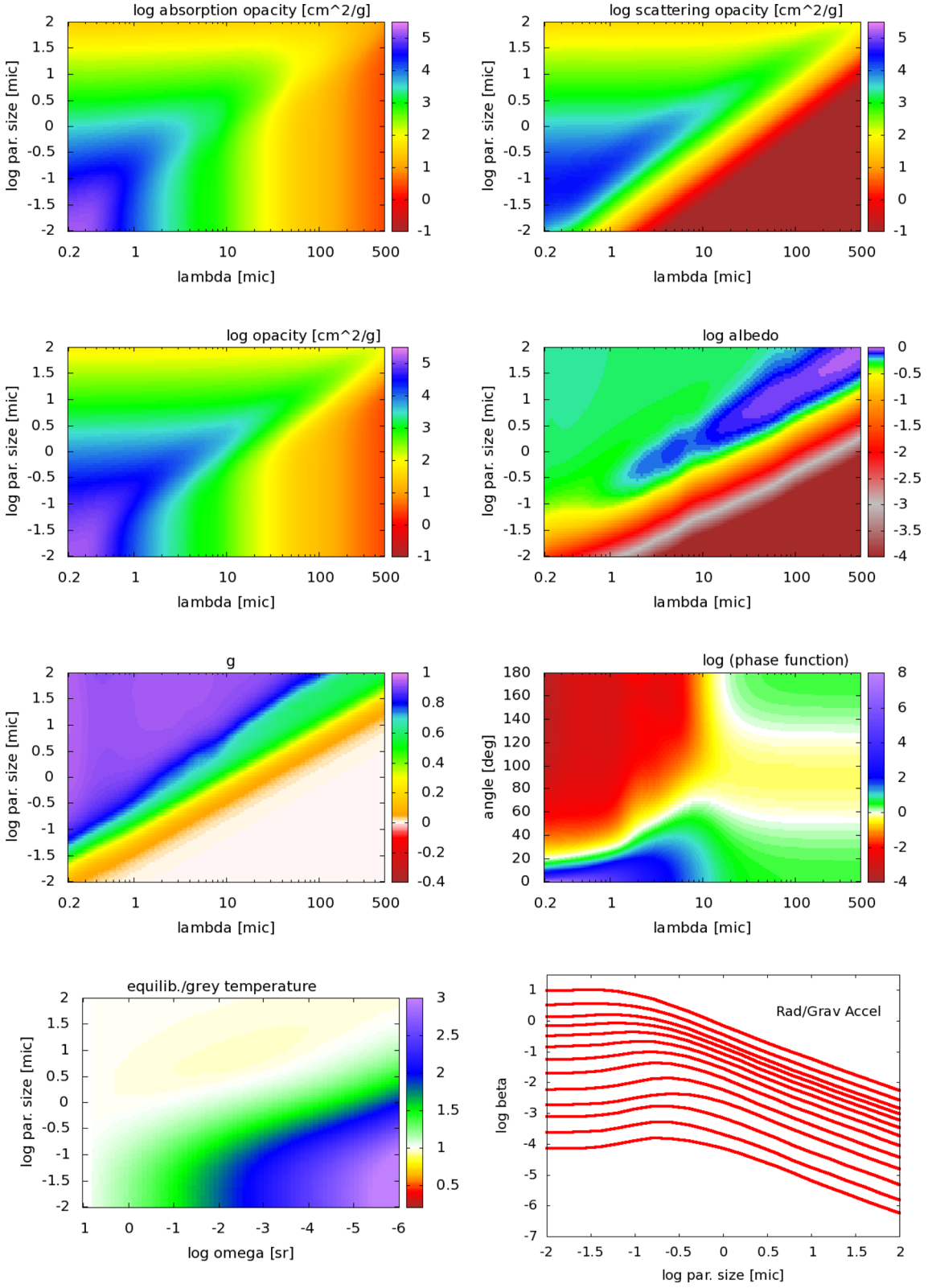

Figure A11. Carbon assuming optical data for 400°C. Pictures and notation are the same as in the previous figure.

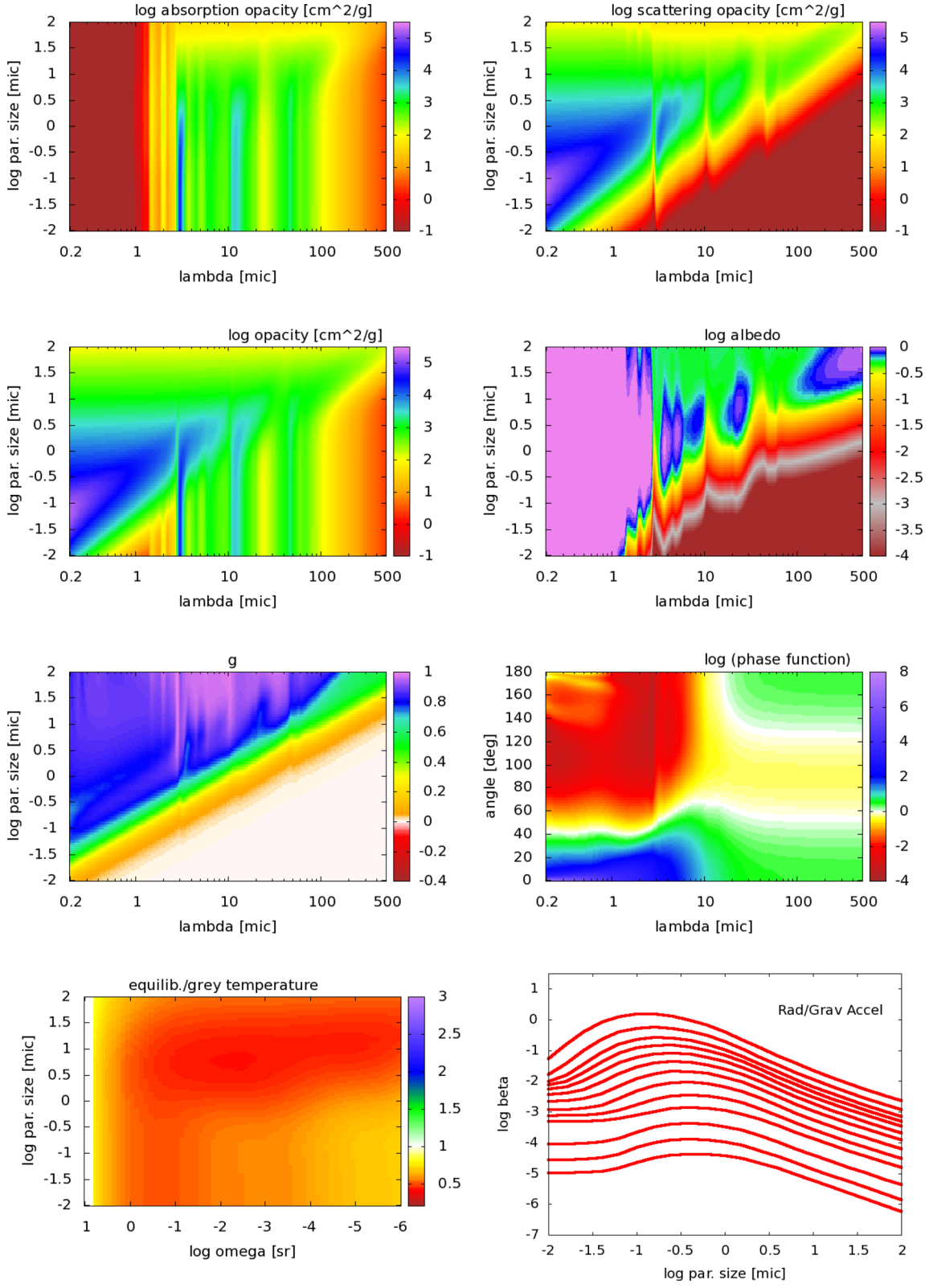

Figure A12. Water ice. Pictures and notation are the same as in the previous figure.

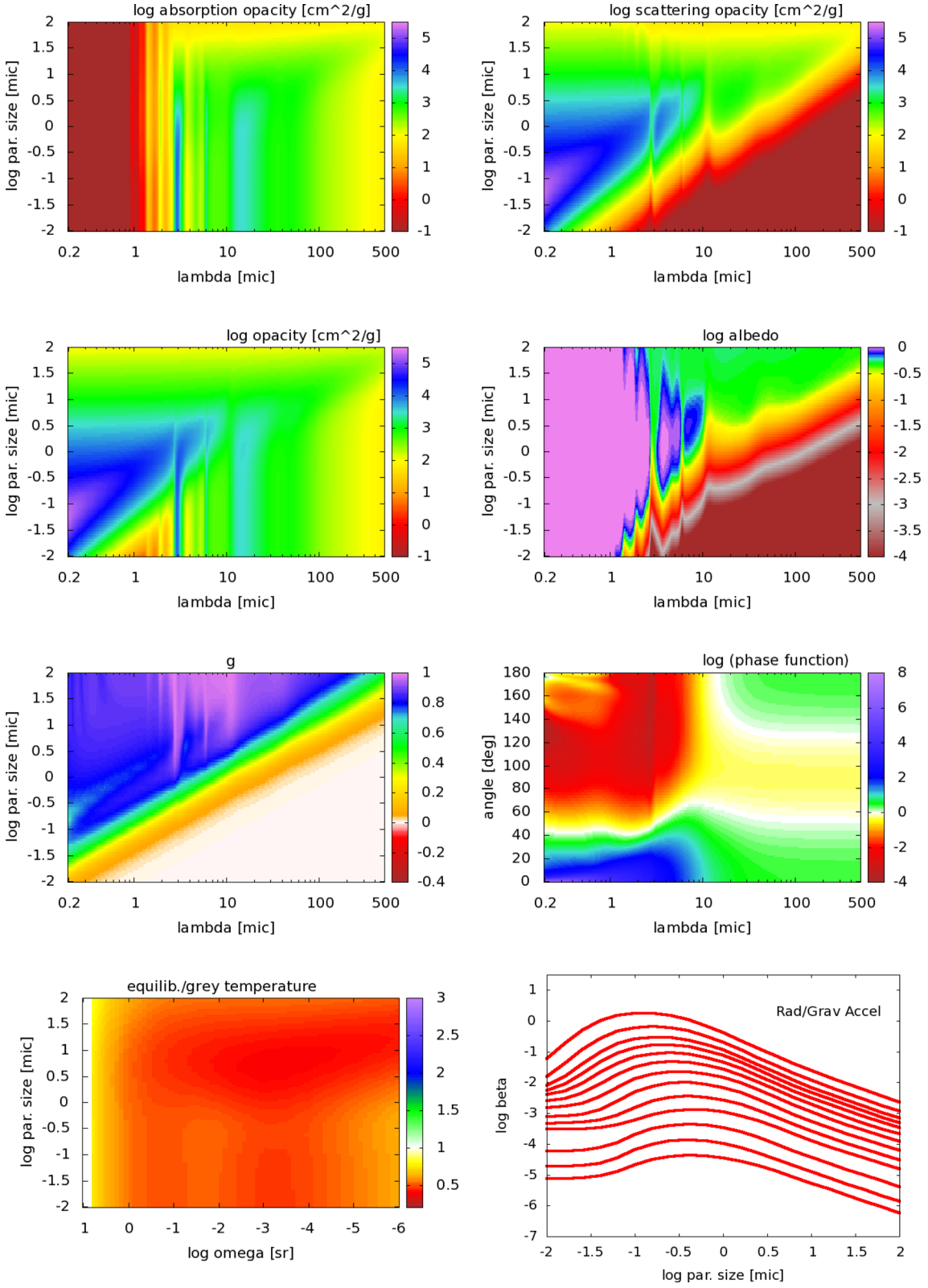

Figure A13. Liquid water. Pictures and notation are the same as in the previous figure.

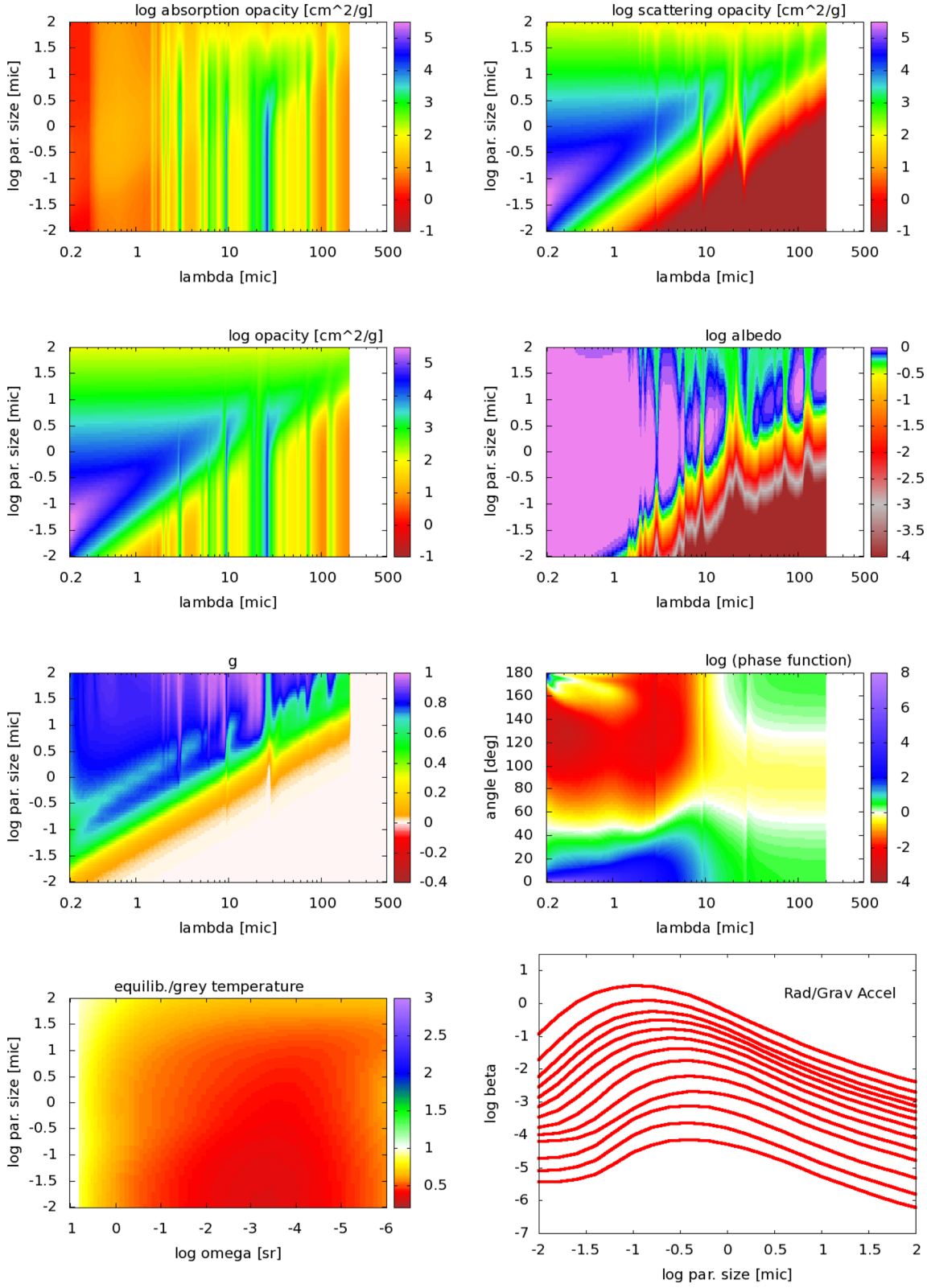

Figure A14. Ammonia. Pictures and notation are the same as in the previous figure.

This paper has been typeset from a TEX/LATEX file prepared by the author.